



**HAL**  
open science

## **A MAVEN Case Study of Radial IMF at Mars: Impacts on the Dayside Ionosphere**

C. M. Fowler, K. G. Hanley, J. Mcfadden, J. Halekas, S. J. Schwartz, C. Mazelle, M. Chaffin, D. Mitchell, J. Espley, R. Ramstad, et al.

### ► **To cite this version:**

C. M. Fowler, K. G. Hanley, J. Mcfadden, J. Halekas, S. J. Schwartz, et al.. A MAVEN Case Study of Radial IMF at Mars: Impacts on the Dayside Ionosphere. *Journal of Geophysical Research Space Physics*, 2022, 127, 10.1029/2022JA030726 . insu-04472238

**HAL Id: insu-04472238**

**<https://insu.hal.science/insu-04472238>**

Submitted on 22 Feb 2024

**HAL** is a multi-disciplinary open access archive for the deposit and dissemination of scientific research documents, whether they are published or not. The documents may come from teaching and research institutions in France or abroad, or from public or private research centers.

L'archive ouverte pluridisciplinaire **HAL**, est destinée au dépôt et à la diffusion de documents scientifiques de niveau recherche, publiés ou non, émanant des établissements d'enseignement et de recherche français ou étrangers, des laboratoires publics ou privés.

Copyright

# JGR Space Physics

## RESEARCH ARTICLE

10.1029/2022JA030726

### Key Points:

- During radial interplanetary magnetic field conditions at Mars, the magnetic barrier forms deep within the dayside ionosphere
- Planetary ions above the magnetic barrier are exposed to solar wind flow and coupled via weak  $\vec{V} \times \vec{B}$  and strong wave particle interactions
- Plasma temperatures are enhanced by factors of 2–10 within the ionosphere; concurrently the dayside ionosphere is significantly eroded

### Correspondence to:

C. M. Fowler,  
[christopher.fowler@mail.wvu.edu](mailto:christopher.fowler@mail.wvu.edu)

### Citation:

Fowler, C. M., Hanley, K. G., McFadden, J., Halekas, J., Schwartz, S. J., Mazelle, C., et al. (2022). A MAVEN case study of radial IMF at Mars: Impacts on the dayside ionosphere. *Journal of Geophysical Research: Space Physics*, 127, e2022JA030726. <https://doi.org/10.1029/2022JA030726>

Received 7 JUN 2022  
Accepted 16 NOV 2022

## A MAVEN Case Study of Radial IMF at Mars: Impacts on the Dayside Ionosphere

C. M. Fowler<sup>1</sup> , K. G. Hanley<sup>2</sup> , J. McFadden<sup>2</sup>, J. Halekas<sup>3</sup> , S. J. Schwartz<sup>4</sup>, C. Mazelle<sup>5</sup> , M. Chaffin<sup>4</sup> , D. Mitchell<sup>2</sup> , J. Espley<sup>6</sup> , R. Ramstad<sup>4</sup> , Y. Dong<sup>4</sup> , and S. Curry<sup>2</sup> 

<sup>1</sup>Department of Physics and Astronomy, West Virginia University, Morgantown, WV, USA, <sup>2</sup>Space Sciences Laboratory, University of California, Berkeley, CA, USA, <sup>3</sup>Department of Physics and Astronomy, University of Iowa, Iowa City, IA, USA, <sup>4</sup>Laboratory of Atmospheric and Space Physics, University of Colorado, Boulder, CO, USA, <sup>5</sup>IRAP, CNRS, UPS, CNES, University of Toulouse, Toulouse, France, <sup>6</sup>NASA Goddard Space Flight Center, Greenbelt, MD, USA

**Abstract** The solar wind interaction with Mars controls the transfer of energy and momentum from the solar wind into the magnetosphere, ionosphere and atmosphere, driving structure, and dynamics within each. This interaction is highly dependent on the upstream Interplanetary Magnetic Field (IMF) orientation. We use in-situ plasma measurements made by the Mars Atmosphere and Volatile Evolution (MAVEN) mission to identify several prominent features that arise when the IMF is aligned approximately parallel or antiparallel to solar wind flow (conditions known as “radial IMF”). In particular, solar wind protons and alphas are observed to directly penetrate down to periapsis altitudes, while the magnetic barrier forms deep within the dayside ionosphere. The MAVEN observations are consistent with either an ionopause-like boundary or diamagnetic cavity forming beneath the barrier, as a consequence of the dense cold ionosphere and the absence of significant crustal magnetic fields at this periapsis location. The planetary ions above the magnetic barrier are exposed to solar wind flow and subsequent mass-loading. The  $\vec{V} \times \vec{B}$  (convective electric field or “ion pickup”) force is weak and highly variable during radial IMF. While wave particle interactions and subsequent wave heating contribute to incorporating the heavy planetary ions into the solar wind flow, the solar wind momentum is not fully deflected around the obstacle and is delivered into the collisional atmosphere. Significant ion heating is observed deep within the dayside ionosphere, and observed ionospheric density and temperature profiles demonstrate that these ion energization mechanisms drive significant erosion and likely escape to space.

**Plain Language Summary** The planets and comets in our solar system are exposed to a barrage of energetic particles emitted by our Sun, known as the solar wind. These particles carry with them a magnetic field, and this magnetic field plays an important role in determining how the solar wind is deflected around these planetary and cometary bodies. We use observations made by a spacecraft orbiting Mars to investigate this interaction when the solar wind magnetic field is oriented in a somewhat unique fashion, aligned in the same direction as the solar wind flow (in contrast to more typical conditions when the solar wind magnetic field is oriented at an angle to the flow direction). In this unique orientation, we find that solar wind particles crash into the dayside atmosphere of Mars, instead of being deflected around the planet. In addition, this magnetic field orientation allows significant solar wind energy to be deposited into the dayside atmosphere via the interaction of generated electric and magnetic fields, with charged particles in the atmosphere. The resulting near space environment at Mars is highly dynamic and disturbed compared to more typical conditions.

### 1. Introduction

Mars does not possess a global dipole magnetic field and therefore the solar wind interacts with the gravitationally bound ionosphere to produce an induced magnetosphere that acts to slow down and deflect the incident supersonic solar wind flow about the planet (Bertucci et al., 2011; Dubinin et al., 2011; Halekas et al., 2017; Nagy et al., 2004). The induced nature of the Martian magnetosphere means that this interaction is highly dependent upon the upstream solar wind conditions, particularly the Interplanetary Magnetic Field (IMF) orientation (Brain et al., 2006; Crider et al., 2004; Fang et al., 2018). In its nominal Parker Spiral configuration, the IMF makes an angle of  $\sim 57^\circ$  to the Mars-Sun line, depending on Mars season and solar activity (Liu et al., 2021). This leads to quasi-perpendicular shock conditions at the nose of the planet that are characterized by a relatively stable plasma and magnetic field environment and the formation of a clear bow shock and magnetosheath (Bale et al., 2005; Mazelle et al., 2004). In addition, on the dayside at Mars several plasma boundaries are collocated beneath the

magnetosheath that act to separate the shocked solar wind plasma from the cold thermal planetary plasma of the ionosphere (Dubinin et al., 1996; Matsunaga et al., 2017). These boundaries include the Magnetic Pileup Boundary (MPB, also known as the outer edge of the magnetic barrier) (Bertucci, Mazelle, Crider, et al., 2003; Vignes et al., 2000), the Induced Magnetosphere Boundary (IMB) (Dubinin et al., 2008; Dubinin, Winningham, et al., 2006), and the Ion Composition Boundary (ICB) (Breus et al., 1991; Sauer et al., 1995). During Parker Spiral IMF conditions, localized quasi-parallel shock conditions that are characterized by highly variable plasma and magnetic field behavior can arise on one flank of the magnetosphere (Burgess et al., 2005; Schwartz & Burgess, 1991). Case studies have demonstrated that low frequency electromagnetic waves generated at the quasi-parallel flank can transmit energy to the underlying ionosphere, driving ion heating, and escape to space (Collinson et al., 2018; Fowler et al., 2018, 2019, 2021).

In contrast, when the IMF is aligned with the solar wind flow ("radial IMF"), quasi-parallel shock conditions are expected to arise across the entire dayside solar wind interaction region and produce a highly variable plasma environment. While recent studies have demonstrated that this foreshock structure is expected to form upstream under such conditions (Collinson et al., 2020; Omidi et al., 2017), detailed data-driven studies are lacking. In particular, the characterization of these conditions, including the importance of additional sources of variability such as exospheric ion pick up, and the impact of such dynamic structure on the underlying ionosphere, are incomplete. At Venus (also unmagnetized like Mars), Phillips et al. (1986) and Du et al. (2009) used magnetometer observations to show that during radial IMF conditions the Venusian magnetosheath becomes dominated by strong and turbulent magnetic fluctuations, while Zhang et al. (2009) showed that the induced Venusian magnetosphere and corresponding magnetic barrier may disappear entirely. A study by Chang et al. (2020) showed that the magnetic barrier at Venus became weak during radial IMF conditions, and the underlying ionosphere demagnetized (i.e., the solar wind magnetic field was unable to penetrate into it).

These previous studies of radial IMF conditions at Mars and Venus have focused on the response of the plasma boundaries to radial IMF but have yet to determine the consequences for the underlying dayside ionosphere, in particular with regard to energy transfer through the solar wind interaction region. In the case study presented here, we evaluate the effect of radial IMF on the Martian dayside ionosphere using the comprehensive plasma measurements made by the Mars Atmosphere and Volatile Evolution (MAVEN) spacecraft and identify several prominent changes that arise in the dayside interaction region, as compared to more typical Parker Spiral IMF conditions. In particular, MAVEN obtains high time cadence, mass resolved, ion (and electron) distribution functions, alongside measurements of all important plasma parameters, which enable us to fully characterize the local plasma environment and identify the physical processes active. This has not been possible prior to MAVEN because previous spacecraft have not flown instrument suites with these capabilities. This event was originally identified based on Emirates Mars Mission observations of patchy proton aurora caused by direct deposition of solar wind protons on the thermosphere (Chaffin et al., 2022). The data analyzed in this study are described in Section 2 and the MAVEN observations are presented in Section 3. Our interpretations and discussion are presented in Section 4 and conclusions are drawn in Section 5.

## 2. Data Sets

Observations analyzed for this case study were made by NASA's MAVEN mission (Jakosky et al., 2015). For this case study (11 August 2021), MAVEN's elliptical orbit had a periaapsis altitude of ~230 km that sampled the dayside ionosphere, and an apoapsis altitude of ~4,360 km that sampled the magnetotail. This study utilizes observations from the Magnetometer (MAG, Connerney et al., 2015), SupraThermal And Thermal Ion Composition (STATIC, McFadden et al., 2015), Solar Wind Ion Analyzer (SWIA, Halekas, Taylor, et al., 2015), Langmuir Probe and Waves (LPW, Andersson et al., 2015), Solar Wind Electron Analyzer (SWEA, Mitchell et al., 2016), and Neutral Gas and Ion Mass Spectrometer (NGIMS, Mahaffy et al., 2015). The data sources for these data sets are listed in the Acknowledgments.

The 3D magnetic field is measured at 32 Hz by MAG, and data are presented in the Mars Solar Orbital (MSO) coordinate system, defined as  $X$  pointing Sunward along the Mars-Sun line;  $Z$  points north out of the ecliptic plane, and  $Y$  completes the right-handed system pointing approximately opposite to Mars' orbital motion. STATIC is an electrostatic top hat analyzer that measures ions from 0.1 eV up to 30 keV in energy. STATIC utilizes a time of flight velocity analyzer to distinguish the major ion species at Mars ( $H^+$ ,  $He^{++}$ ,  $O^+$ ,  $O_2^+$ , and  $CO_2^+$ ). Observations of solar wind ions are provided at 4 s cadence by SWIA, an electrostatic top hat analyzer.

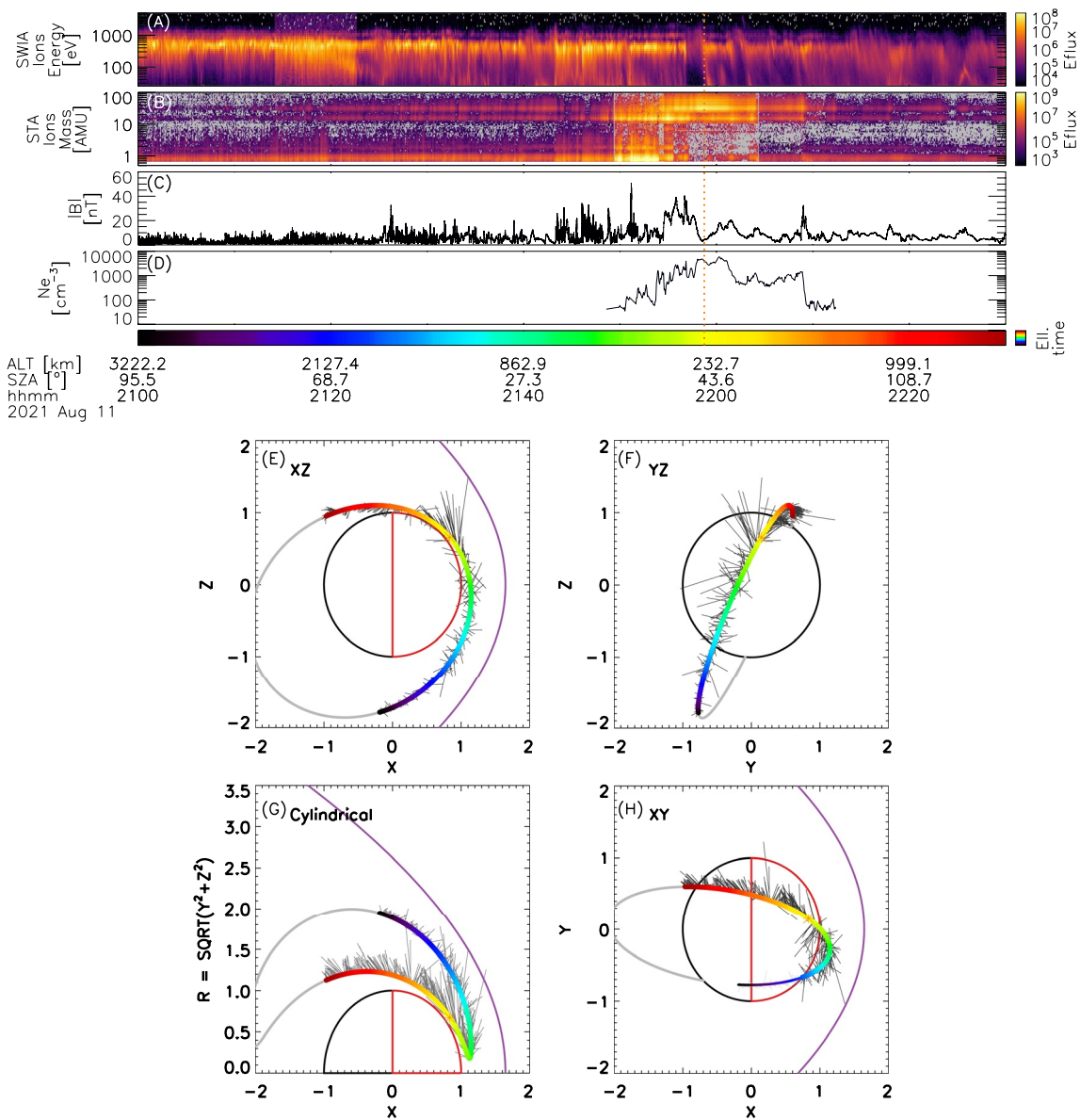


**Figure 1.** Overview of the case study event. Panels show (a) SWIA omni-directional ion energy spectrogram; (b) STATIC mass spectrogram; (c) magnetic field amplitude; and (d) ionospheric thermal electron density. MAVEN's orbit in various planes of the MSO coordinate system is shown in panels (e–h); the gray whiskers denote the magnetic field vector in each plane; the purple conic marks the average position of the bow shock derived by Vignes et al. (2000). Eflux has units of  $\text{eV} (\text{eV s sr cm}^2)^{-1}$ . The rainbow color bar (under panel d) can be directly compared to the orbit tracks and rainbow color bars in all subsequent figures.

Thermal electron density and temperature are provided by LPW via the analysis of current-voltage curves (Ergun et al., 2015, Ergun, Andersson, Fowler, & Thaller, 2021; Ergun, Andersson, Fowler, Thaller, & Yelle, 2021). Observations of suprathermal electrons at energies 3 eV–4 keV are provided by SWEA, an electrostatic top hat analyzer. NGIMS is a quadrupole mass spectrometer that measures neutral and ion densities at  $\sim 2$  s cadence.

### 3. Observations: Case Study on 11 August 2021

#### 3.1. Overview

An overview of the case study is shown in Figure 1. Panels (a–d) show time series plasma observations made by MAVEN during the periapsis pass, while panels (e–h) show MAVEN's orbit trajectory in various planes of the MSO coordinate system. Prior to 21:40, MAVEN is sampling in the dayside dawn southern hemisphere of the

magnetosphere and observes high amplitude fluctuations in the ion energy flux (panel a) and the magnetic field strength (panel c). These characteristics permeate the entire time range shown and are characteristic of in-situ plasma measurements made through quasi-parallel shock crossings at Earth (e.g., Burgess et al., 2005) and Mars (e.g., Fowler et al., 2019; Halekas et al., 2017; Ruhunusiri et al., 2017). As is discussed later, MAVENs orbit does not sample the foreshock region during this case study, and for the remainder of this paper, we refer to this highly dynamic region that MAVEN samples as the “interaction region.” One can argue that the Mars-solar wind interaction starts upstream of the bow shock and continues through the ionosphere—for this study, we are referring to the magnetosheath region that displays high amplitude nonlinear wave features. Panels (e–h) show that MAVEN is well below the typical bow shock location and likely sampling downstream of an extended foreshock. During this initial time period, MAVEN observes solar wind protons, alphas, and planetary heavy ions (panels a and b). As MAVEN approaches periapsis (~21:40–21:50) the spacecraft passes close to the subsolar point (SZA values approaching zero) and highly variable plasma conditions are still observed. At around 21:50, MAVEN encounters the thermal plasma of the ionosphere (panel d), coincident with increases in heavy planetary ion fluxes (panel b). The ionospheric plasma density profile is characterized by significant variability (panel d) through till periapsis (orange vertical line). On the outbound segment (~22:00–22:15), MAVEN is sampling in the northern hemisphere close to the dusk terminator polar region. The ionospheric density and magnetic field profiles are still variable but less disturbed than on the inbound segment. The magnetic field whiskers shown in panels (e–h) demonstrate significant variability particularly during the inbound segment, further supporting the notion that MAVEN is sampling a dynamic environment here.

### 3.2. Particle Observations

Detailed time series plasma observations focusing on the inbound segment of this periapsis pass are shown in Figure 2. Prior to MAVEN encountering the ionosphere at ~21:50, the ion composition is a mixture of solar wind ions and energized planetary  $O^+$  and  $O_2^+$  (panels f–i). Observations of ions traveling in the  $-X$  MSO direction made by SWIA (i.e., Marsward, panel i) demonstrate that several populations exist: a solar wind beam-like proton population at ~500 eV; a solar wind beam-like alpha population at ~1,000 eV, and shocked protons and alphas spanning 10s eV up to ~1 keV. SWIA's finer energy resolution allows it to distinguish the solar wind alphas in energy, while STATIC's mass resolution confirms this composition. Panel DF1 shows a STATIC energy-mass distribution function observed at the first blue vertical line demonstrating that the protons, alphas, and heavy planetary ions have broad distributions in energy. SWIA observes solar wind protons and alphas traveling in the  $-X$  MSO direction throughout the entire periapsis pass. Accompanying suprathermal electron observations are characterized by energy spectra containing significant fluxes at high energy (>70 eV) that are typically associated with magnetosheath and/or solar wind plasma (panel c). These populations are observed throughout the periapsis pass. Suprathermal electron energy spectra associated with the cold ionosphere (characterized by reduced fluxes above energies of 70 eV) are observed only sporadically around periapsis. The heavy planetary ions that are present during this inbound segment have energies of tens of eV up to a few hundred eV (panels g and h) and are characterized by densities up to  $40 \text{ cm}^{-3}$  (panel e). Their energy spectra (panels g and h) are characterized by large variability in energy, and the distributions are broad in energy.

As MAVEN encounters the thermal ionosphere at ~21:50, the ion composition becomes dominated by  $O^+$  and  $O_2^+$ , and thermal electron densities are  $\sim 100 \text{ cm}^{-3}$  (panels d and e). Energy spectra of  $O^+$  and  $O_2^+$  in this region (panels g and h) demonstrate significant variability that is coincident in time with the variability observed in thermal density (panel d). A STATIC ion distribution function sampled at the second vertical blue line from this region is shown in panel DF2. Low energy (<100 eV) planetary protons, ions of  $amu/q$  (mass-to-charge) of two, and heavy ions are observed. The  $amu/q$  two ions are likely  $H_2^+$  because (a) they are low energy and MAVEN is sampling the ionosphere and (b) the presence of a “ghost peak” at  $amu/q \sim 12$  in DF2 is consistent with the presence of  $H_2^+$  (see Section 3.8 in McFadden et al. [2015]). STATIC's energy sweep spans up to 500 eV during this time period and the lower energy portion of solar wind protons are visible at energies of a few hundred eV; solar wind alphas are not visible as they would have energies of ~1,000 eV, outside of the energy sweep range here. We note that the background calibration software did not fully remove the instrumental signatures of straggling protons (see McFadden et al., 2015), which are observed at solar wind proton energies (~500 eV) at higher mass bins in DF2. We believe the unique and highly variable nature of the observations are the cause of this, but these stragglers are easily discernible and do not influence our conclusions.

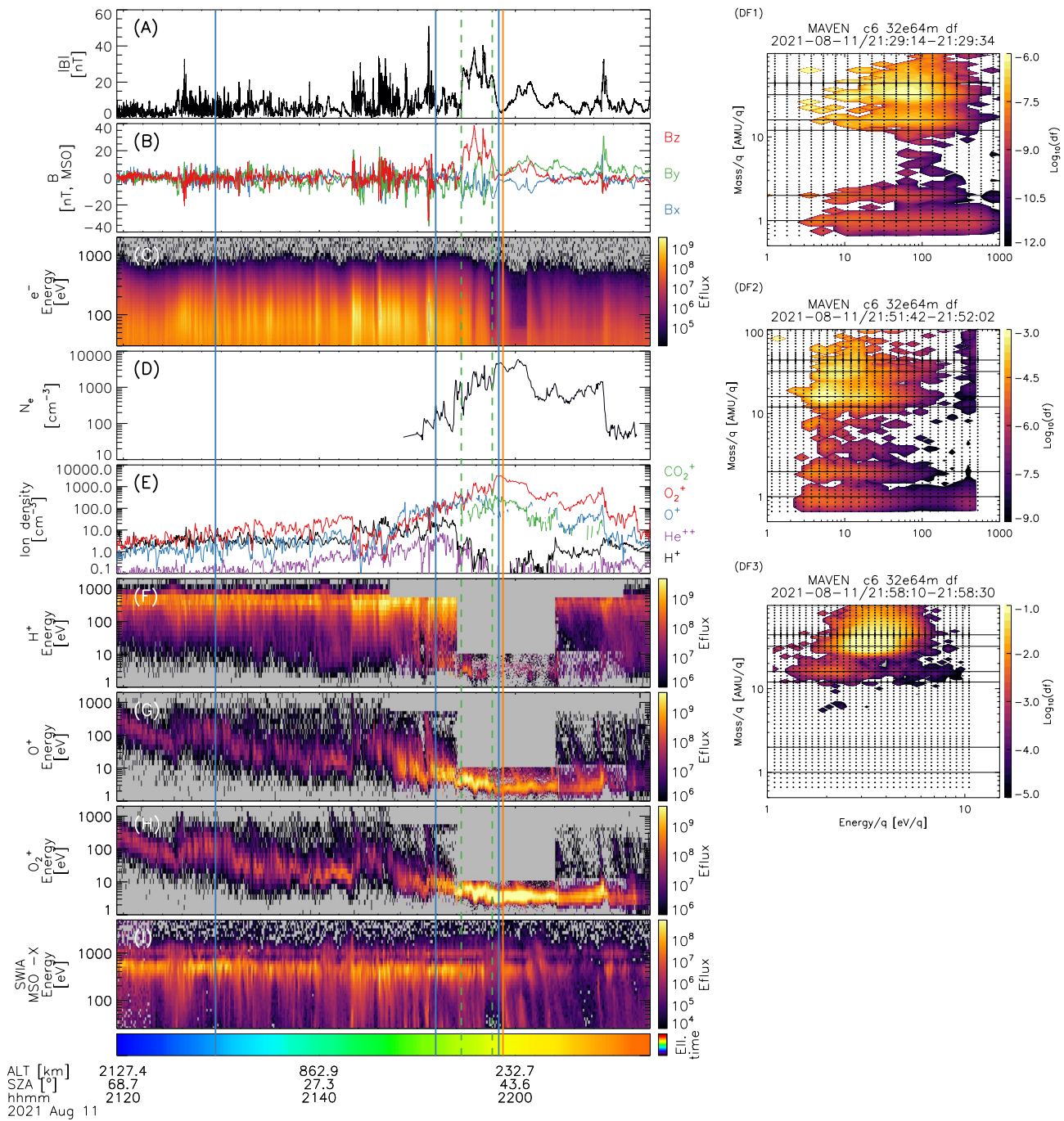


**Figure 2.** Time series plasma observations of the periapsis pass analyzed. Panels show (a and b) magnetic field magnitude and vector; (c) SWEA suprathermal electron energy flux; (d) thermal electron density; (e) STATIC ion density; (f–h) STATIC energy spectra for H<sup>+</sup>, O<sup>+</sup> and O<sub>2</sub><sup>+</sup>; (i) SWIA ion energy spectrogram in the anti-sunward direction (–X MSO). The orange line is periapsis (~230 km), the green vertical dashed lines mark the magnetic barrier (see Section 4.4). (DF1–DF3): ion distribution functions measured by STATIC at the three blue vertical lines. DF has units of (km<sup>3</sup> s<sup>–3</sup> cm<sup>3</sup>)<sup>–1</sup>.

As MAVEN progresses through to periapsis, ionospheric densities are still highly variable and increase up to ~5,000 cm<sup>–3</sup> (panels d and e). The planetary ion population is observed as the low energy beam in panels (g and h), and the distribution function obtained at the third blue vertical line (panel DF3) confirms that O<sub>2</sub><sup>+</sup> dominates the ion composition here. The observed ion distributions are broad in energy and temperatures are significantly enhanced by factors of ~2 compared to typical values (discussed in Section 4.5). Note that because STATIC's

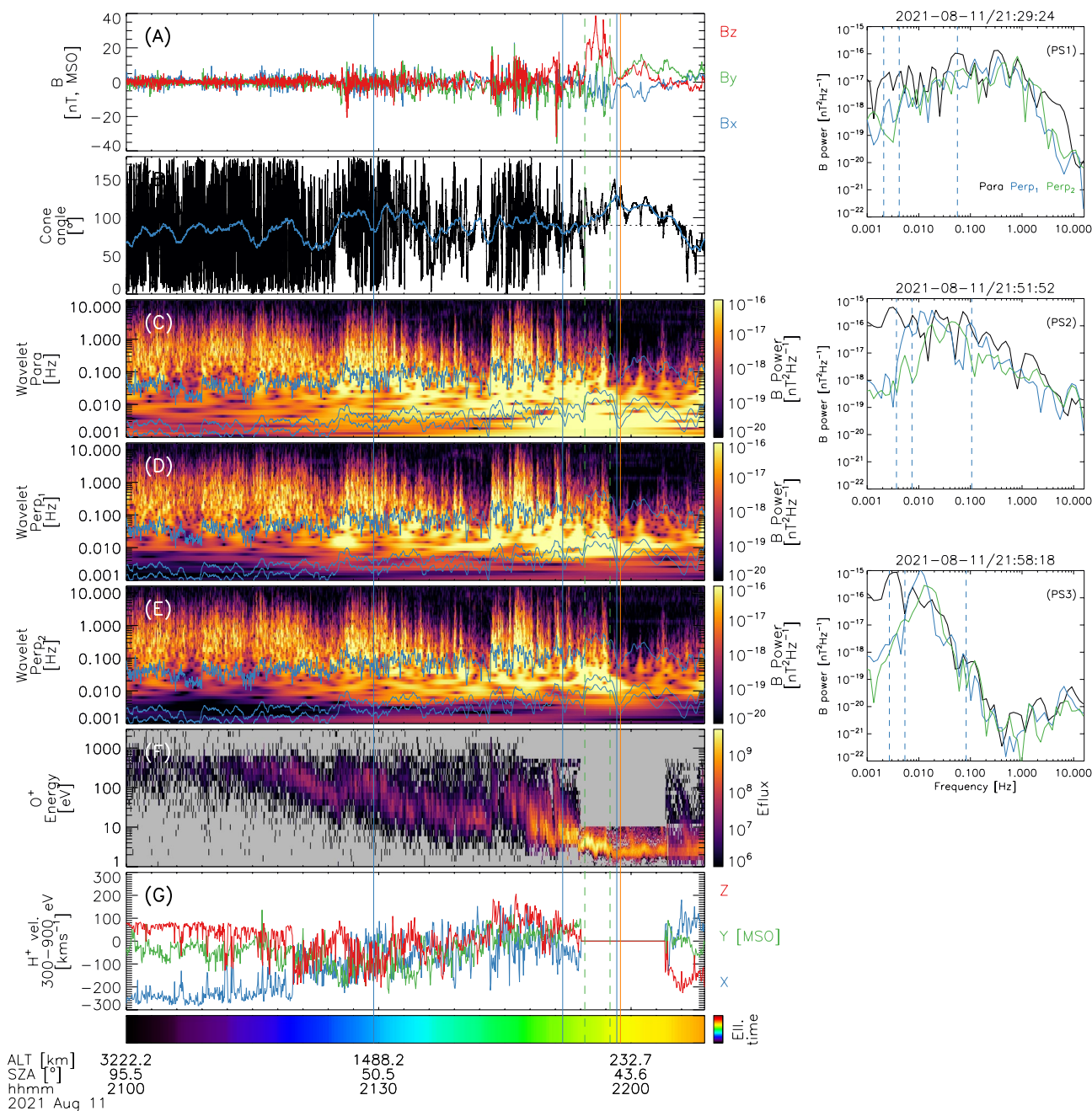


**Figure 3.** Time series plasma observations focusing on the magnetic fluctuations observed upstream of Mars during the inbound segment. Panels show (a) magnetic field vector; (b) cone angle between the magnetic field and +X MSO (Sunward) direction (the blue line is the average calculated over a 90 s sliding window); (c–e) wavelet transforms of the three magnetic field components (parallel, perpendicular 1 and 2), the blue lines show the  $H^+$ ,  $O^+$  and  $O_2^+$  cyclotron frequencies; (f) STATIC  $O^+$  energy spectrum; (g) solar wind  $H^+$  velocity derived from STATIC. The inserts PS1–PS3 show power spectra from panels (c–e), measured at each of the three vertical blue lines.

energy sweep spanned 1–10 eV at periapsis, STATIC did not observe the more energetic solar wind protons and alphas that SWIA observed here (panel i).

### 3.3. Magnetic Field Fluctuations

Detailed time series observations of the magnetic field during the event are shown in Figure 3. The magnetic field vector measurements (panel a) demonstrate that significant rotations in the magnetic field accompany the

fluctuations during the inbound segment, especially prior to the first vertical dashed green line located just after 21:54 (the dashed green vertical lines are discussed in detail in Section 4.4). The cone angle between the magnetic field and the +X MSO direction (Mars-Sun line) is shown in panel b, where values of 0° and 180° denote magnetic field pointing sunward and anti-sunward, respectively, and values of 90° denote magnetic field aligned perpendicular to the Mars-Sun line. The blue line shows the average cone angle calculated over a 90-s sliding window. A 90-s window is chosen to be consistent with the magnetic field analysis described below. The cone angle is highly variable and while the average value in the interaction region lies between ~50° and 120°, there are frequent excursions to values close to 0° and 180°. Variability, particularly at higher frequencies, in the cone angle decreases substantially past the first dashed green vertical line, and the importance of this is discussed in Section 4.4.

Wavelet transforms of the components of the magnetic field are shown in panels (c–e). The magnetic field observations are rotated into the average frame of the magnetic field using a 90-s sliding window, and the wavelet transforms are computed using the method described in Torrence and Compo (1998). Prior to MAVEN entering the ionosphere, the proton cyclotron period is approximately 30 s, and we chose a 90-s sliding window to encompass roughly three proton cyclotron wave periods. Panel (c) shows wave power in the component parallel to the magnetic field (“para”); panels (d and e) show wave power in the two components perpendicular to the magnetic field (“perp<sub>1</sub>” and “perp<sub>2</sub>”). Higher frequency ( $\geq 0.1$  Hz) fluctuations are observed in all three magnetic field components in the interaction region; after the second dashed green vertical line magnetic fluctuations at higher frequencies are not observed. As MAVEN enters the ionosphere (around the first dashed green vertical line), significant wave power is observed in all three components at lower frequencies ( $\lesssim 0.01$  Hz) and some of this is likely attributable to the changes in a large-scale magnetic field structure observed in panel (a) rather than “real waves.”

The blue lines that overplot the wavelet spectra in panels (c–e) mark the local H<sup>+</sup>, O<sup>+</sup>, and O<sub>2</sub><sup>+</sup> cyclotron frequencies in the spacecraft frame. Significant wave power exists at the H<sup>+</sup> cyclotron frequency in all three magnetic field components in the region upstream from the ionosphere, with wave power gradually increasing as MAVEN approaches the ionosphere. Prior to ~21:15, wave power is also observed in the parallel component of the magnetic field at the heavy ion (O<sup>+</sup> and O<sub>2</sub><sup>+</sup>) cyclotron frequencies (panel c). In contrast, no significant wave power is observed at the heavy ion cyclotron frequencies in the two perpendicular components (panels d and e) until after ~21:15; wave power at these frequencies then tends to grow in amplitude in all three components as MAVEN approaches the ionosphere. The appearance of perpendicular wave power at the heavy ion cyclotron frequencies at ~21:15 coincides with when heavy ions are first observed by STATIC (panel f). The inserts PS1–PS3 show power spectra observed at the three solid blue vertical lines; PS1 and PS2 are observed in the interaction region and confirm the presence of higher frequency waves and wave power at the heavy ion cyclotron frequencies. PS3 is observed as MAVEN enters the ionosphere and shows that wave power at higher frequencies is greatly reduced here.

The bulk flow velocity of H<sup>+</sup> is shown in panel (g), calculated for proton energies between 300 and 900 eV (the energy range within which the bulk of the solar wind proton flow is observed in Figure 2f). Significant small-scale variability is observed in the magnitude and direction of the flow in the interaction region. Prior to ~21:20, the H<sup>+</sup> bulk flow is predominantly in the anti-Sunward direction (–X MSO); at this time there is a clear change in the flow characteristics suggesting that MAVEN is transitioning between flow regimes as it passes from the outer to inner magnetosphere (e.g., Figures 1e–1h). This transition occurs at the same time that heavy ions are first observed by STATIC.

#### 4. Discussion

Here, we discuss the most prominent features of the Mars-solar wind interaction that arise during this case study. As we will justify following, we infer that radial IMF conditions are the primary driver of these features. MAVEN did not sample the pristine solar wind during this time period (confirmed in both the time series data and Figures 1e–1h), and so we cannot say conclusively that radial IMF conditions were present during this case study. We can, however, make a compelling argument that this was the case based on the MAVEN observations, and that in fact the observations are very difficult to explain if nominal Parker Spiral IMF conditions are invoked. These details are discussed below.

#### 4.1. Penetration of Solar Wind Protons and Alphas Through Periapsis: Evidence for Radial IMF

The presence of Marsward traveling solar wind protons and alpha particles throughout the periapsis pass is extremely atypical and suggests a very different Mars-solar wind interaction compared to normal Parker Spiral IMF conditions. The energy fluxes of these protons and alphas are 2–3 orders of magnitude greater than those associated with “penetrating protons,” solar wind protons that penetrate the dayside ionosphere via charge exchange interactions with the hydrogen corona upstream of the Martian bowshock and the dayside neutral atmosphere (Halekas, Lillis, et al., 2015). In addition, penetrating protons are most abundantly observed below altitudes of ~200 km (Henderson et al., 2021) and during Mars southern solstice (Mars solar longitude  $L_s = 270^\circ$ ) when the hydrogen exosphere is most dense (Halekas, 2017). MAVEN’s periapsis altitude for this pass is 230 km and observations are made close to aphelion ( $L_s = 84^\circ$ ). These characteristics strongly indicate that penetrating protons are not the cause of the observed solar wind protons and alphas here.

As already noted, the highly variable plasma environment during the inbound segment is reminiscent of conditions that arise under quasi-parallel shock conditions. During this time range, MAVEN is sampling close to the subsolar point and as such quasi-parallel shock conditions would constitute near-radial IMF conditions. Our interpretation is that radial IMF conditions are present, resulting in an extended foreshock spanning the upstream region ahead of Mars, and that MAVEN is sampling downstream of this extended foreshock. Because MAVEN does not sample the pristine solar wind on this orbit, we cannot conclusively confirm this; however, the observations (those noted here and those discussed in the following sections) provide strong and consistent support for this interpretation.

#### 4.2. Mass Loading of the Solar Wind Flow by Planetary Ions

As the solar wind flow approaches Mars, it will be subject to a variety of forces that determine if and how the flow is deflected around the planetary obstacle. The two-fluid momentum equations for solar wind protons and heavy planetary ions (i.e., heavy ions sourced from the planetary ionosphere) can be written as follows (Chapman & Dunlop, 1986; Halekas et al., 2017):

$$\vec{F}_p = m_p n_p \left( \frac{\partial}{\partial t} + \vec{V}_p \cdot \nabla \right) \vec{V}_p = \frac{n_p}{n_e} \left[ q n_p (\vec{V}_p - \vec{V}_h) \times \vec{B} + \vec{J} \times \vec{B} - \nabla P_e \right] - \nabla \cdot \vec{P}_p \quad (1)$$

$$\vec{F}_h = m_h n_h \left( \frac{\partial}{\partial t} + \vec{V}_h \cdot \nabla \right) \vec{V}_h = \frac{n_h}{n_e} \left[ q n_h (\vec{V}_h - \vec{V}_p) \times \vec{B} + \vec{J} \times \vec{B} - \nabla P_e \right] - \nabla \cdot \vec{P}_h \quad (2)$$

where, subscripts  $p$ ,  $h$ , and  $e$  denote protons, heavy ions, and electrons, respectively, and all other symbols have their usual meaning. Equations 1 and 2 incorporate fluid particle pressure (via scalar electron pressure  $P_e$  and tensor ion pressure  $\vec{P}_p$ ,  $\vec{P}_h$ ) and the  $\vec{J} \times \vec{B}$  force terms (which can be separated into the magnetic pressure and curvature terms in the usual fashion). Momentum coupling between the protons and heavy ions is captured by the  $\vec{V} \times \vec{B}$  term, where the definition of velocity depends specifically upon the difference between the proton and heavy ion velocity vectors.

The  $\vec{J} \times \vec{B}$  and pressure terms cannot be calculated using single point measurements but statistical studies by Halekas et al. (2017) and Ramstad et al. (2020) have shown that the  $\vec{V} \times \vec{B}$  term typically dominates at Mars by roughly an order of magnitude. Heavy ions are usually sourced from either the ionization of the extended neutral corona of Mars (Deighan et al., 2015) or from the ionosphere itself, and in both cases the initial heavy ion velocity can typically be assumed to be negligible compared to the solar wind flow in the planetary frame. Thus, momentum coupling via the  $\vec{V} \times \vec{B}$  term acts to incorporate the heavy ions into the solar wind flow, a process more commonly referred to as ion pickup (or laminar pickup, e.g., Szegő et al., 2000), and which is particularly important for unmagnetized bodies that possess a gravitationally bound atmosphere, including comets, Venus, and Mars (e.g., Coates, 2004; Ip & Axford, 1986; Luhmann & Kozyra, 1991). We note here that the term “convective electric field” is perhaps a more accurate description of this force, because ion pickup can still occur even when  $\vec{V}$  is parallel to  $\vec{B}$ . Gary (1993) demonstrates that field-aligned beam distributions of newborn ions in the solar wind frame are unstable to wave generation and can subsequently be picked up by the solar wind as a result of wave-particle interactions. As expanded on below, this pickup mechanism is also consistent with the MAVEN

observations. For simplicity, for the remainder of this paper, we stick with the commonly used term ion pickup to describe the  $\vec{V} \times \vec{B}$  force, noting the above caveats.

For the case of radial IMF, the  $\vec{V} \times \vec{B}$  term is expected to be small and one can then ask the question of which physical processes facilitate the transfer of momentum between solar wind protons and heavy ions, as the latter are incorporated into the solar wind flow. This is a particularly interesting question because the  $\vec{J} \times \vec{B}$  and pressure terms in Equations 1 and 2 do not explicitly couple the two ion populations. As we discuss further below, the MAVEN observations do indeed provide evidence of weak  $\vec{V} \times \vec{B}$  coupling and suggest that wave particle interactions and subsequent heating of the ion populations play a more dominant role in isotropizing and thermalizing the proton and heavy ion distributions for this case study.

MAVEN observes  $O^+$  and  $O_2^+$  ions on the inbound segment. In the upstream region at times prior to  $\sim 21:52$  (roughly the second blue vertical line in Figures 2g and 2h), the heavy ion energies are relatively low (typically 10s to 100s eV) compared to more typical keV pickup ion energies under nominal Parker Spiral IMF conditions (e.g., Rahmati et al., 2017), and they exhibit significant variability in both energy and energy flux. Further, the heavy ions flow (with significant variability) at approximately  $90^\circ$  to the solar wind protons (not shown here). These characteristics are consistent with the heavy ions being accelerated by a small and highly variable  $\vec{V} \times \vec{B}$  force, as expected given the observed variability in the magnetic field vector during these radial IMF conditions. Further evidence of heavy ion acceleration via motional electric field is observed as MAVEN encounters the dense thermal plasma in Figure 2, DF2: second, higher energy populations of  $O^+$  and  $O_2^+$  exist at energies of  $\sim 10$ – $20$  eV and  $25$ – $40$  eV, respectively, that enter STATIC from different directions compared to lower energy ( $\lesssim 10$  eV) thermal ions.

Evidence for wave heating facilitating momentum transfer between the ion populations is observed in the ion distribution functions measured in the interaction region (Figures 2g, 2h, 2DF1, and 2DF2), which possess extended suprathermal tails in the energy dimension for all ions. Significant fluctuations are observed in the parallel and perpendicular magnetic field components coincident in time with these heated ion populations (Figures 3c–3f, 3PS1, and 3PS2). These magnetic field fluctuations are likely produced from a combination of sources: (a) ultralow frequency (ULF) waves generated upstream within the foreshock (the region that MAVEN does not sample) that are transmitted through the quasi-parallel shock into the downstream region that MAVEN samples and (b) waves generated locally in the downstream region as a result of plasma micro-instabilities.

In the upstream region, low frequency waves can be generated by newly born pickup ions and the reflection of ions from the quasi-parallel shock back upstream (in the foreshock). In the former case, newly born pickup ions will form a high-speed beam (with velocity  $-V_{sw}$ , where  $V_{sw}$  is the solar wind velocity) in the solar wind frame and the ion distribution is nearly equivalent to a two-species plasma where the solar wind core protons and pickup ions (including heavies) can be represented by two drifting Maxwellian distributions separated by significant velocities (in this case, to first order, the solar wind velocity). In the latter case, ions reflected back upstream will constitute a similar situation albeit with a larger separation in drift velocities. In both cases, the newly picked up ions act as a source of free energy and the nature of the resulting instability depends upon  $\alpha$ , the angle between the solar wind flow and solar wind magnetic field (e.g., Section 8 of Gary [1993], Brinca and Tsurutani [1989], Scholer and Terasawa [1990], and Brinca [1991]). The resulting waves act to disrupt the beam of  $\sim$ stationary heavy ions and to isotropize them in the solar wind frame (i.e., incorporate them into the solar wind flow). For radial IMF conditions,  $\alpha$  will be small and in the frame of the solar wind the newly picked up ions form a beam distribution traveling at  $\sim -V_{sw}$ , in contrast to a ring-beam distribution when  $\alpha \gtrsim 45^\circ$ . Studies of, and computer simulations based upon, spacecraft observations made in the environments of comets Halley and Giacobini-Zinner have shown that for the tenuous cometary ion density the ion/ion right hand resonant instability is the dominant growing mode for newborn ions picked up under small  $\alpha$  (Gary et al., 1989; Glassmeier et al., 1989; Tsurutani & Smith, 1986). In the case of small  $\alpha$ , the combination of the cyclotron resonance conditions and Doppler shift means that the instability will appear as fluctuations at the corresponding ion-cyclotron frequency in the spacecraft frame (e.g., Tsurutani & Smith, 1986 and Section 7 in Gary [1991]). This has led to the clear identification of heavy-water-ion/proton right hand instabilities at the heavy-water-ion cyclotron frequency, during  $\alpha \lesssim 60^\circ$  conditions, in cometary environments (Glassmeier et al., 1989; Tsurutani et al., 1987, 1989), along with the so called “proton cyclotron waves” at Venus and Mars (Bertucci et al., 2013; Delva et al., 2011, 2015; Romanelli et al., 2016).

In contrast, waves generated from protons backstreaming after reflecting from the quasi-parallel shock will travel with velocity greater than  $-V_{sw}$  in the solar wind frame, and the resulting waves are not expected to be generated at exactly the proton-cyclotron frequency (Gary, 1993). The conditions present during radial IMF at Mars (and inferred to exist here) are analogous to the aforementioned cometary environment and are consistent with the above mechanisms generating ULF waves both upstream (via ion pickup and reflection from the quasi-parallel shock) and downstream (via ion pickup) of the foreshock. Waves generated upstream can be transmitted through the quasi-parallel shock (e.g., Shan et al., 2014, 2020) where they are observed by MAVEN. In their linear stage, these waves are primarily transverse and take on a quasi-sinusoidal form, and MAVEN is likely sampling these waves at a later non-linear stage in their evolution after transmission through the quasi-parallel shock, explaining why wave power at the ion cyclotron frequencies does not dominate the perpendicular wavelet power spectra shown in Figures 3PS1 and PS2. Thus, the dynamic wave environment observed by MAVEN in the interaction region may be a combination of these processes, and we have not attempted to quantify the contributions from each mechanism here.

Finally, the small scale size of Mars' magnetosphere relative to important plasma length scales (e.g., the proton gyro radius) means that the solar wind plasma is not expected to fully thermalize before encountering the planet (Moses et al., 1988). The interaction region that MAVEN samples downstream of the quasi-parallel shock is thus also likely unstable to the local generation of plasma waves via micro-instabilities that will contribute to the electromagnetic wave environment. Sources for such waves include temperature anisotropies (Harada et al., 2016; Ruhunusiri et al., 2015) and relative drifts between solar wind and heavy planetary ions (Akbari et al., 2022).

### 4.3. Penetration of Solar Wind Protons and Alphas Through Periapsis: The Role of Physical Collisions in the Atmosphere

The observation of solar wind protons and alphas traveling Marsward in the ionosphere at MAVEN's periapsis demonstrates that the solar wind flow has not been fully deflected around Mars by the usual electromagnetic and pressure gradient forces associated with the magnetosphere during Parker Spiral IMF conditions. An interesting question then arises: Do physical collisions with the neutral atmosphere act to stop the solar wind flow? To determine whether this process is feasible and consistent with the MAVEN observations, we show several parameters related to the neutral atmosphere, and collisions between the solar wind protons and this atmosphere, in Figure 4. Panel (a) shows neutral O and CO<sub>2</sub> densities measured by NGIMS on the inbound segment of this periapsis. The straight lines are fits to these density profiles, made assuming constant scale heights for each species, and extrapolated down to the planet surface. The extrapolated values are consistent with NGIMS measurements made earlier in the mission when MAVEN's periapsis reached as low as ~125 km (Benna et al., 2015), giving us confidence in the fits and extrapolations.

Panel (b) shows calculated collision frequencies between solar wind protons and neutral O and CO<sub>2</sub>, using collision frequencies defined in Tables 4.4 and 4.5 in Schunk and Nagy (2009). The total collision frequency is the sum of these two. Panel (c) shows estimates for the distance solar wind protons travel in the ionosphere between physical collisions with the neutral atmosphere, using two different methods. The first assumes that solar wind protons travel at 300 km s<sup>-1</sup> (based on Figures 2i and 3g), and that the distance traveled between physical collisions is equal to the proton speed divided by the total collision frequency shown in Figure 4b. These results are shown as the black line in Figure 4c. The second method calculates the mean free path ( $\lambda$ ) of solar wind protons traveling through the atmosphere via Equation 3:

$$\lambda = \frac{1}{(\sigma_{po}n_o + \sigma_{pco2}n_{co2})} \quad (3)$$

where,  $n_o$  and  $n_{co2}$  are the O and CO<sub>2</sub> densities, respectively;  $\sigma_{po}$  is the cross section for H<sup>+</sup> – O collisions, taken to be  $1 \times 10^{-15}$  cm<sup>-2</sup> (Figures 1 and 6 in Hamre et al. (1999) and Pandey et al. (2007), respectively); and  $\sigma_{pco2}$  is the cross section for the H<sup>+</sup> – CO<sub>2</sub> collision, taken to be  $1 \times 10^{-15}$  cm<sup>-2</sup> (Figure 4 in López-Patiño et al. [2015]). The mean free path of solar wind protons calculated using method two is shown as the blue line in Figure 4c.

As expected, the distances traveled by solar wind protons in between collisions with the neutral atmosphere are large (100's–1,000's km) at higher altitudes ( $\geq 200$  km) and reduce in value quickly as the neutral densities increase at lower altitudes. We have assumed that the solar wind proton flow is effectively stopped when the distance traveled between collisions reduces to 1 km, and the altitudes at which this criterion is met for each

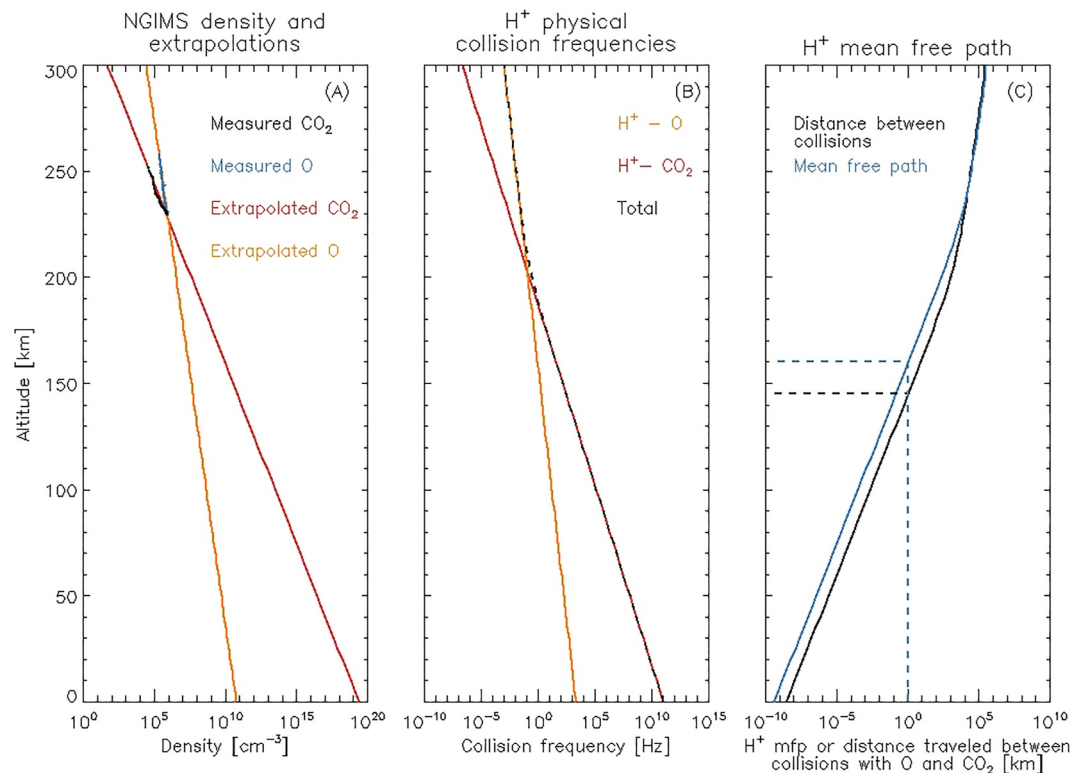


**Figure 4.** Observations and parameters calculated pertaining to the neutral atmosphere and its ability to stop solar wind protons. Panels show: (a) measured O and CO<sub>2</sub> density profiles, along with fitted profiles extrapolated to the surface; (b) calculated collision frequencies between solar wind protons and the neutral profiles shown in panel (a); (c) calculated parameters showing (1) the distance solar wind protons travel between collisions (black line, based on panel b); (2) the mean free path of protons in the atmosphere (blue line, based on Equation 3).

method are marked by the dashed black and blue lines in the figure. Under these assumptions, the solar wind proton flow is stopped between altitudes of ~145–160 km, far below MAVEN's periapsis altitude of 230 km for this orbit. Photochemical modeling and detailed analysis of NGIMS observations have shown that the exobase region (the transition from transport-dominated processes above to collision-dominated processes below) typically lies between 180 and 200 km at Mars (e.g., Fox & Hać, 2009; Jakosky et al., 2017; Nier & McElroy, 1977). The results and trends from both methods are thus consistent with each other and our general understanding of photochemical processes and collisions in the Martian atmosphere.

#### 4.4. Magnetic Barrier Formation

During Parker Spiral IMF conditions, a clear magnetic barrier typically forms at the top of the ionosphere that acts to separate the shocked solar wind plasma from the cold ionospheric plasma. This barrier, known as the magnetic pileup boundary (MPB), is identified through a combination of plasma characteristics: (a) a sharp increase in magnetic field strength; (b) a rotation in the magnetic field to a draped configuration about the ionosphere; (c) a reduction in magnetic fluctuations downstream of the boundary; (d) a reduction in energetic (>70 eV) suprathermal electron fluxes; and (e) a sharp transition in ion composition from shocked solar wind/magnetosheath proton dominated to cold heavy planetary ion dominated (e.g., Bertucci et al., 2005; Breus et al., 1991; Dubinin, Fränz, et al., 2006; Vignes et al., 2000; Xu et al., 2016).

The observations in Figure 2 demonstrate that the magnetic barrier does not form at the top of the ionosphere: at ~21:50 (thermal plasma is first observed, panel d) the magnetic field is still highly variable (panel a), there is no large-scale rotation in the field (panel b), significant fluxes of energetic suprathermal electrons are present (panel c), and there is no clear switch in the ion composition (panel e). For this case study, the magnetic barrier appears to form deep within the dayside ionosphere and our identification of this barrier is enclosed by the green dashed

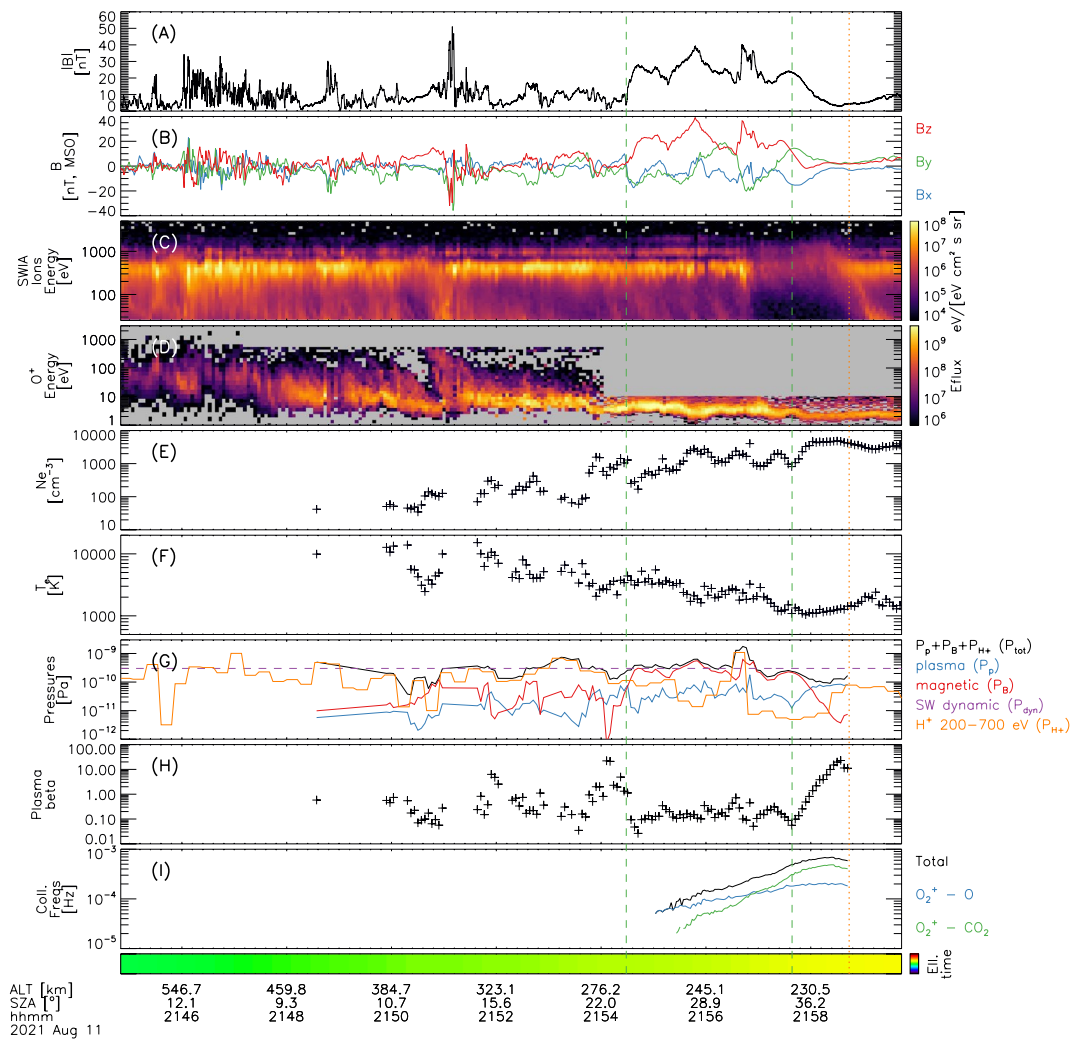


**Figure 5.** Time series plasma observations focused on the magnetic barrier that forms within the ionosphere on the inbound segment. Panels show: (a and b) magnetic field strength and vector; (c) SWIA ion energy spectrum; (d) STATIC O<sup>+</sup> energy spectrum; (e and f) LPW thermal electron density and temperature; (g) pressure contributions; (h) plasma beta (thermal plasma pressure divided by magnetic pressure); (i) collision frequencies between O<sub>2</sub><sup>+</sup> and the neutral atmosphere. The dashed green vertical lines enclose the magnetic barrier; the dotted orange vertical line marks periapsis.

vertical lines in Figures 2, 3, and 5. Referring to Figure 2, at the upper boundary (first dashed green vertical line), there is an enhancement in magnetic field strength and a large-scale rotation in the field to a draped configuration (panels a and b). At the lower boundary (second dashed green vertical line), there is a reduction in magnetic field fluctuations (panel a) and reduction in energetic suprathermal electrons (panel c). The magnetic field strength also decreases below the boundary, from ~25 nT to ~3 nT, over an altitude range of ~3 km, suggesting the presence of an ionopause-like boundary or diamagnetic-like cavity, the former having been observed at Venus and Mars (e.g., Elphic et al., 1980; Duru et al., 2009) and the latter at comets (e.g., Goetz, Koenders, Richter, et al., 2016; Holmberg et al., 2019). We discuss this feature below.

The magnetic barrier spans an altitude range of 267 km down to 232 km and is situated deep within the thermal ionosphere: significant plasma density close to 1,000 cm<sup>-3</sup> is observed immediately above this barrier, which is directly exposed to the incident solar wind flow. For comparison, the magnetic barrier at these SZA is typically located at altitudes of ~900 km (Vignes et al., 2000) and at these altitudes and SZA the ionospheric plasma densities are typically 2–3 orders of magnitude smaller (Fowler et al., 2022). The cold ionospheric plasma above the magnetic barrier is directly exposed to the solar wind flow and can be mass loaded into it, as described in Section 4.2. While the magnetic barrier prevents the IMF from being convected deeper into the ionosphere, solar

wind protons and alphas are observed by SWIA to penetrate beneath the magnetic barrier due to their large gyro radii that are on the order of several hundred kilometers for the observed plasma conditions.

In Section 4.3, we demonstrated that physical collisions between solar wind protons and the neutral atmosphere will stop the solar wind flow at around 150 km altitude, well below MAVENs periapsis altitude (230 km) and the altitude at which the magnetic barrier is observed (232–267 km). An interesting question that then arises from these observations is: Why does the magnetic barrier form at the altitudes observed, given that the solar wind flow is observed to reach significantly lower altitudes in the atmosphere and will not be stopped until well beneath the magnetic barrier?

To answer this question a zoom in on the magnetic barrier is shown in Figure 5. Various plasma observations and parameters calculated from the MAVEN data are shown, including various pressure terms (panel g), the plasma beta (panel h), and various collision frequencies (panel i). The total pressure (shown in panel g) is calculated via Equation 4:

$$P_{tot} = P_p + P_B + P_{H^+} = N_e k_b T_e + \frac{B^2}{2\mu_0} + \rho V_{H^+}^2 \quad (4)$$

where, the first term on the right hand side represents the thermal electron pressure, the second term the magnetic pressure, and the third term the dynamic pressure from solar wind protons flowing in the  $-X$  MSO direction into the ionosphere.  $N_e$ ,  $T_e$  and  $B$  are the measured thermal electron density and temperature, and magnetic field strength, respectively;  $k_b$  is the Boltzmann constant and  $\mu_0$  the permeability of free space. Because the term  $\rho V_{H^+}^2$  represents the dynamic pressure from solar wind ions traveling in the  $-X$  MSO direction in the ionosphere,  $V_{H^+}$  is equal to  $280 \text{ km s}^{-1}$ , equivalent to protons at 400 eV energy, the energy of these solar wind protons in the ionosphere, as observed by SWIA in Figure 5c. The mass density  $\rho = m_p n_{H^+}$ , where  $m_p$  is the proton mass and  $n_{H^+}$  is the density of solar wind ions observed by SWIA between energies of 200 and 700 eV, centered around the beam energy of 400 eV. We assume that solar wind protons dominate the solar wind mass composition here as inclusion of the solar wind alpha contribution does not affect our conclusions. These pressure contributions are shown in panel (g) along with an estimate of the upstream pristine solar wind dynamic pressure as the purple dashed line (“SW dynamic,”  $P_{dyn}$ ).  $P_{dyn}$  was estimated based on observations prior to 21:20 when MAVEN observes a sharp change in the flow conditions as it approaches Mars. We have used a solar wind density of  $2 \text{ cm}^{-3}$  (Figure 2e) and a solar wind velocity of  $300 \text{ km s}^{-1}$  (Figure 3g) to obtain this dynamic pressure estimate.

Referring back to Figure 5, prior to encountering the magnetic barrier (first dashed green vertical line),  $P_{dyn}$  dominates the pressure contribution as expected.  $P_{H^+}$  is approximately equal to  $P_{dyn}$  here, giving us confidence that our assumptions in calculating  $P_{H^+}$  are appropriate. When the magnetic barrier is first encountered (first dashed green vertical line),  $P_{H^+}$  decreases and  $P_B$  increases to become the dominant pressure term. This switch in pressure dominance is consistent with expectations at the MPB (Holmberg et al., 2019).  $P_{H^+}$  decreases as MAVEN traverses through the magnetic barrier. The solar wind proton beam energy does not change significantly meaning that the solar wind proton velocity remains constant and the density decreases through the magnetic barrier. Some solar wind protons are thus likely deflected around the ionosphere, but significant fluxes are still observed beneath the barrier. At the lower boundary of the magnetic barrier (second dashed green vertical line)  $P_B$  decreases and  $P_p$  increases, and there is a clear switch to thermal plasma pressure dominance. The thermal plasma pressure increases by roughly an order of magnitude beneath the magnetic barrier, driven by the observed increase in thermal electron density. The plasma beta (defined as thermal plasma pressure divided by the magnetic pressure, panel h) is consistent with these trends.

The switch in dominance of magnetic to plasma pressure at the lower edge of the magnetic barrier is reminiscent of an ionopause boundary. Ionopause boundaries are features of unmagnetized bodies that separate hot magnetosheath plasma above from cold thermal ionospheric plasma beneath via pressure balance. The magnetic pressure dominates above an ionopause boundary as a result of magnetic field pileup; this magnetic pressure typically balances the upstream solar wind dynamic pressure. Beneath the ionopause boundary, the thermal plasma pressure dominates and balances the impinging magnetic pressure from above, preventing the solar wind magnetic field from convecting into the ionosphere. Ionopause boundaries are regularly observed at Venus (e.g., Bertucci, Mazelle, Slavin, et al., 2003; Luhmann & Cravens, 1991) and somewhat less so at Mars (e.g., Sánchez-Cano et al., 2020; Vogt et al., 2015). While Mars does possess significant crustal magnetic fields that can lead to magnetic pressure dominating within the ionosphere, MAVEN's periapsis for this case study is far from any

**Table 1**  
*Measured Plasma Parameters Used to Calculate the Required Radial Neutral Wind Speed for a Diamagnetic Cavity to Form*

Parameter	Location 1: lower edge of magnetic barrier	Location 2: minimum in magnetic field strength
$N_e$ (cm <sup>-3</sup> )	825	4,750
$T_e$ (K)	1,180	1,330
$B_1$ (nT)	25	25
$B_2$ (nT)	3	3
$\partial r$ (km)	3	3
$\nu_{in}$ (Hz)	0.0005	0.0007
$u_i$ (ms <sup>-1</sup> ) (assumed)	0	0
$u_n$ (ms <sup>-1</sup> )	0.4	0.05

*Note.* Parameters are listed for two locations: (1) at the lower edge of the magnetic barrier (second dashed green vertical line in Figure 5); (2) at the minimum in magnetic field strength just prior to periapsis (just prior to the dotted orange vertical line in Figure 5).  $B_1$  and  $B_2$  are the change in magnetic field strength, which occur over a radial distance  $\partial r$ .

strong crustal field sources and the formation of an ionopause is feasible. Total pressure is conserved across the magnetic barrier in this case study, a characteristic consistent with ionopause boundaries. A minor discrepancy is that there is typically little to no thermal ionospheric plasma observed above an ionopause and this is not the case here: Figure 5d shows the large thermal electron densities (values close to 1,000 cm<sup>-3</sup>) present above the magnetic barrier, marking this as an atypical potential ionopause boundary.

A second possibility to explain the observations is that the depletion in magnetic field strength below the magnetic barrier is caused by the formation of a cometary diamagnetic cavity. Cometary diamagnetic cavities (also features of unmagnetized bodies) have been observed at comets Halley and Giacobini-Zinner (e.g., Cravens et al., 1995; Goetz, Koenders, Hansen, et al., 2016) and also separate hot magnetosheath plasma from cold ionospheric plasma, but not via pressure balance. Instead magnetic pressure above the cavity (again resulting from magnetic field pileup) is balanced by ion-neutral drag within the cavity. The outgassing of cometary material produces a radially outward flow of neutrals that collide with its ionized constituents (the cometary ionosphere), producing the outward drag force that balances the impinging magnetic pressure force via Equation 5 (Cravens, 1987):

$$-\frac{\partial}{\partial r} \left( \frac{B^2}{8\pi} \right) = n_e m_i \nu_{in} (u_i - u_n) \quad (5)$$

where, the left hand term represents the radial change in magnetic pressure across the diamagnetic cavity boundary;  $m_i$  is the ion mass, here assumed to be that of O<sub>2</sub><sup>+</sup> which is the dominant ion in the Martian ionosphere (Figure 2e);  $\nu_{in}$  is the total ion-neutral collision frequency, calculated as the sum of the O<sub>2</sub><sup>+</sup> – O and O<sub>2</sub><sup>+</sup> – CO<sub>2</sub> collision frequencies using Table 4.4 in Schunk and Nagy (2009); and  $u_i$  and  $u_n$  are the ion and neutral radial wind speeds, respectively.

We can rearrange Equation 5 to solve the radial neutral wind  $u_n$  that would be required for a diamagnetic cavity to form. MAVEN measures all required parameters and these are shown in Table 1 for two locations: (a) at the lower boundary of the magnetic barrier (the second dashed green vertical line) and (b) at the point of minimum magnetic field strength below the magnetic barrier (21:58:32 UTC), just prior to periapsis (the orange dotted vertical line).

We have assumed that the radial ion wind ( $u_i$ ) is zero here. The MAVEN-STATIC instrument (which is capable of measuring vertical or horizontal ion winds depending upon its orientation) was flown such that it could measure horizontal ion winds for this particular periapsis pass; however, vertical ion winds measured by STATIC are typically negligible. The resulting estimates of  $u_n$  are small, <1 ms<sup>-1</sup>. While horizontal neutral winds are expected to dominate at Mars (with values up to ~100 ms<sup>-1</sup>, Bougher et al., 2015; Roeten et al., 2019), the requirement of such small radial/vertical neutral winds makes the formation of a diamagnetic cavity feasible.

To summarize our findings here, the formation of an ionopause-like boundary or a cometary diamagnetic cavity are both consistent with the MAVEN observations to explain why the magnetic barrier forms at the observed altitude. The clear switch from magnetic to plasma pressure dominance at the lower edge of the magnetic barrier perhaps favors the formation of an ionopause-like boundary, but as noted above, the presence of significant thermal plasma above this boundary is atypical.

#### 4.5. Enhanced Ion Temperatures at Periapsis

The ion distribution function in Figure 2DF3 shows that the dominant ion species, O<sub>2</sub><sup>+</sup>, possesses a suprathermal tail in the energy dimension. As will be shown in Section 4.6, the corresponding O<sub>2</sub><sup>+</sup> temperature is enhanced by a factor of ~2 compared to more typical values, indicating that even at periapsis the thermal plasma has been significantly energized. The cause of this heating beneath the magnetic barrier is not yet known; one hypothesis is that the direct penetration of solar wind protons into the cold, stationary, dense ionosphere may drive a two-stream instability that leads to this heating. An ongoing and separate study is investigating the plausibility of

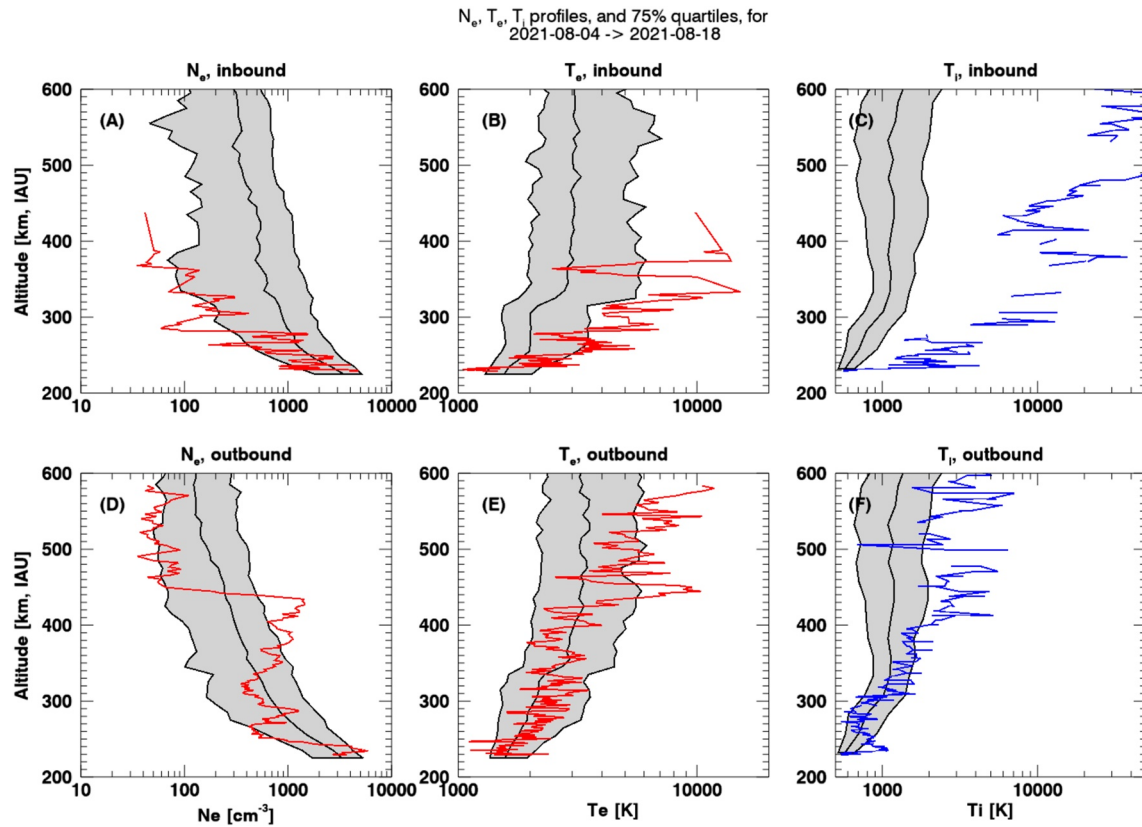


**Figure 6.** Statistical medians of thermal electron density and temperature, and  $O_2^+$  temperature, over the 2-week time period centered on the case study orbit (96 periapsis passes). Gray regions enclose the 25th and 75th quartiles and the middle black lines mark the median values. Red and blue lines are the values observed during the case study orbit.

this hypothesis. Periapsis altitude is 230 km for this case study, somewhat higher than the typical exobase altitude range of  $\sim 180$ – $200$  km, and so it is unclear whether this ion heating extends through the exobase region or not.

#### 4.6. Severely Eroded Dayside Ionosphere

We have compared the observed ionospheric densities and temperatures for this case study pass to the typical statistical profiles observed by MAVEN during the 2-week period centered on this event. The results are shown in Figure 6; the gray outlines enclose the lower and upper 25% quartiles of each quantity, and the middle black lines represent the median values of each. The gray outlines and median values are generated from 96 separate periapsis passes covered by the time range noted in the figure title. The red and blue lines are profiles measured for this case study. The dayside ionospheric density profile is severely eroded (panel a): the upper boundary of the ionosphere extends to about 450 km altitude, far below the typical values that extend above 600 km. Ionospheric density is reduced by an order of magnitude at some altitudes and by factors of 2–3 at periapsis. The dayside electron temperature profile (panel b) is significantly elevated throughout the periapsis pass, enhanced by factors of 2–5 compared to the median value. The  $O_2^+$  temperature is enhanced by even greater amounts, factors of  $>2$  at periapsis and approaching an order of magnitude at 450 km altitude. At higher altitudes, the ion temperature represents that of the mass loaded ions and is even further enhanced. The plasma density and temperature profiles exhibit significant variability, and all of these characteristics support the interpretation that significant energization of the dayside ionosphere is occurring.

In contrast, density and temperature profiles measured on the outbound segment of the orbit (bottom row) that are made over the terminator region and in the magnetotail demonstrate far less deviation from the statistical expectations. All three profiles still contain noticeable variability, but this variability lies for the most part within

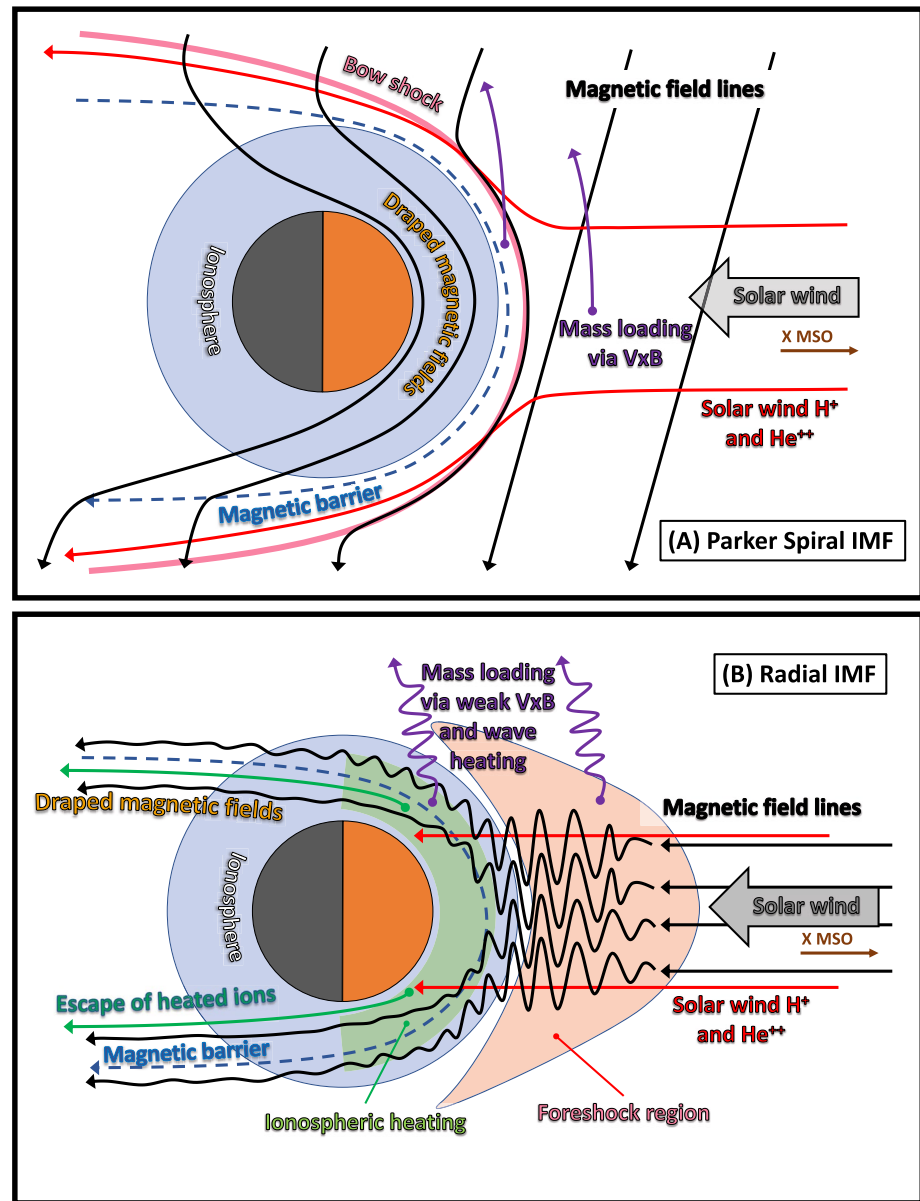


**Figure 7.** Schematics of the Mars-solar wind interaction during Parker Spiral and radial IMF conditions. The Parker Spiral configuration is based on previous works, for example, McComas et al. (1986).

the quartile ranges. An ionopause-like feature appears to be present at  $\sim 450$  km altitude (panel d) although we have not investigated this further.

## 5. Interpretation and Conclusions

We have analyzed MAVEN time series plasma observations from a case study where unique and highly variable plasma conditions exist over the dayside Mars-solar wind interaction region. While MAVEN did not sample the pristine solar wind during this event, observed plasma environment characteristics and prominent features provide strong support that radial IMF conditions were present. The presence of radial IMF substantially changes the Mars-solar wind interaction and appears to drive significant erosion of the dayside ionosphere. Our interpretations are summarized below and in Figure 7. The Mars-solar wind interaction during Parker Spiral IMF conditions is depicted in Figure 7a, based upon earlier studies such as McComas et al. (1986): a bow shock forms upstream of Mars that decelerates and deflects the solar wind flow around the obstacle, and the magnetic barrier

separates the shocked solar wind plasma from the cold planetary ions. The Mars-solar wind interaction during radial IMF conditions, as inferred from this study, is depicted in Figure 7b. The key conclusions are summarized as follows:

1. A highly variable plasma environment is observed upstream over the sub-solar point, which is reminiscent of quasi-parallel IMF conditions that would constitute radial IMF. Our interpretation is that MAVEN is sampling downstream of an extended foreshock region ahead of Mars.
2. Mars-ward traveling solar wind protons and alphas are observed to penetrate down to MAVEN periapsis altitudes (230 km), suggesting that the typical electromagnetic and pressure gradient forces associated with the magnetosphere under Parker Spiral IMF conditions do not fully deflect the solar wind flow around the planetary obstacle.
3. Physical collisions between flowing solar wind protons and the neutral atmosphere are expected to stop the solar wind flow at around 150 km altitude, well below MAVEN's periapsis altitude.
4. The magnetic barrier (or MPB) forms deep within the dayside ionosphere (232–267 km altitude), and the presence of an ionopause-like boundary or cometary diamagnetic cavity beneath it can explain its formation.
5. Significant densities of thermal ionospheric plasma ( $n_e \sim 1,000 \text{ cm}^{-3}$ ) are present above the magnetic barrier and are directly exposed to the solar wind flow. Exposed planetary ions are therefore mass loaded into the solar wind flow. The momentum coupling between solar wind flow and heavy planetary ions is usually facilitated by the  $\vec{V} \times \vec{B}$  force (convective electric field or “ion pickup”); however, this force is weak and highly variable during the observed radial IMF conditions. As a result, wave particle interactions play a much larger role in coupling the ion species and incorporating the heavy planetary ions into the solar wind flow. Observed ion distribution functions are consistent with weak acceleration via  $\vec{V} \times \vec{B}$  and strong heating via wave particle interactions.
6. The plasma conditions and wave environment are consistent with the generation of ultralow frequency waves upstream in the foreshock via ring beam instabilities, driven by newly born pickup ions and ions reflected from the quasi-parallel shock. These waves evolve into nonlinear states as they are transmitted through the quasi-parallel shock and observed by MAVEN. The generation of waves locally downstream of the quasi-parallel shock due to micro-instabilities likely also contributes to the electromagnetic wave environment. The small scale size of Mars' magnetosphere and the subsequent inability of the solar wind plasma to fully thermalize provides free energy for this.
7. Thermal ion distribution functions observed just above the exobase region possess suprathermal energy tails and their corresponding temperatures are enhanced by a factor of two compared to average conditions, suggesting that significant energy is deposited from the solar wind into the deep dayside ionosphere.
8. The dayside ionosphere is severely eroded compared to average conditions: the upper ionosphere extends to only 450 km altitude (compared to >600 km on average) and ionospheric densities are reduced by up to an order of magnitude below this. Corresponding ionospheric plasma temperatures are enhanced by factors of 2–10. Significant and atypical variability in plasma density and temperature is observed down to periapsis (~230 km altitude), close to the exobase region.

Further study is required to answer outstanding questions that have arisen from this study, and the utilization of global simulations of the solar wind interaction would be highly advantageous here. For example, outstanding questions include the following: (a) Does the observed case study represent all configurations of the Mars-solar wind interaction during radial IMF conditions or can other configurations occur? (b) What is the nature and extent of the inferred upstream foreshock region that forms under radial IMF conditions? (c) What are the changes (if any) to global ion escape rates under radial IMF conditions?

Radial IMF conditions appear to drive substantial changes in the Mars-solar wind dayside interaction region, including in ionospheric plasma structure, dynamics, erosion, and escape to space. These results provide insight into how Mars and the ionospheres of unmagnetized bodies in general (e.g., Mars, Venus, and comets) interact with the solar wind when the IMF is aligned with the solar wind flow. In addition, this study highlights the importance of dedicated solar wind monitors at planets: in this case, such observations would enable us to unambiguously characterize the upstream solar wind conditions that drive the observed conditions in the dayside ionosphere.

## Data Availability Statement

MAVEN data are publicly available at the NASA Planetary Data System (PDS, <https://pds.nasa.gov/>) and the MAVEN Science Data Center (<https://lasp.colorado.edu/maven/sdc/public/>). Ion densities and temperatures provided by MAVEN-STATIC are available via the Space Physics Environment Data Analysis Software (SPEDAS, <https://spedas.org/blog/>).

## Acknowledgments

Work at WVU and SSL was supported by NASA funding for the MAVEN project through the Mars Exploration Program under Grant NNH10CC04C. We thank the anonymous reviewers for their time and effort in providing feedback and helping to improve this manuscript.

## References

- Akbari, H., Newman, D., Fowler, C., Pfaff, R., Andersson, L., Malaspina, D., et al. (2022). Micro-scale plasma instabilities in the interaction region of the solar wind and the Martian upper atmosphere. *Journal of Geophysical Research: Space Physics*, 127(5), e2022JA030591. <https://doi.org/10.1029/2022ja030591>
- Andersson, L., Ergun, R., Delory, G., Eriksson, A., Westfall, J., Reed, H., et al. (2015). The Langmuir probe and waves (LPW) instrument for MAVEN. *Space Science Reviews*, 195(1), 173–198. <https://doi.org/10.1007/s11214-015-0194-3>
- Bale, S., Balikhin, M., Horbury, T., Krasnoselskikh, V., Kucharek, H., Möbius, E., et al. (2005). Quasi-perpendicular shock structure and processes. *Space Science Reviews*, 118(1), 161–203. <https://doi.org/10.1007/s11214-005-3827-0>
- Benna, M., Mahaffy, P., Grebowsky, J., Fox, J. L., Yelle, R. V., & Jakosky, B. M. (2015). First measurements of composition and dynamics of the Martian ionosphere by MAVEN's neutral gas and ion mass spectrometer. *Geophysical Research Letters*, 42(21), 8958–8965. <https://doi.org/10.1002/2015gl066146>
- Bertucci, C., Duru, F., Edberg, N., Fraenz, M., Martinez, C., Szego, K., & Vaisberg, O. (2011). The induced magnetospheres of Mars, Venus, and Titan. *Space Science Reviews*, 162(1–4), 113–171. <https://doi.org/10.1007/s11214-011-9845-1>
- Bertucci, C., Mazelle, C., Acuna, M., Russell, C., & Slavin, J. (2005). Structure of the magnetic pileup boundary at Mars and Venus. *Journal of Geophysical Research*, 110(A1), A01209. <https://doi.org/10.1029/2004ja010592>
- Bertucci, C., Mazelle, C., Crider, D., Vignes, D., Acuña, M., Mitchell, D., et al. (2003). Magnetic field draping enhancement at the Martian magnetic pileup boundary from Mars global surveyor observations. *Geophysical Research Letters*, 30(2), 1099. <https://doi.org/10.1029/2002gl015713>
- Bertucci, C., Mazelle, C., Slavin, J., Russell, C., & Acuna, M. (2003). Magnetic field draping enhancement at Venus: Evidence for a magnetic pileup boundary. *Geophysical Research Letters*, 30(17). <https://doi.org/10.1029/2003gl017271>
- Bertucci, C., Romanelli, N., Chaufray, J.-Y., Gomez, D., Mazelle, C., Delva, M., et al. (2013). Temporal variability of waves at the proton cyclotron frequency upstream from Mars: Implications for Mars distant hydrogen exosphere. *Geophysical Research Letters*, 40(15), 3809–3813. <https://doi.org/10.1002/grl.50709>
- Bougher, S., Pawlowski, D., Bell, J., Nelli, S., McDunn, T., Murphy, J., et al. (2015). Mars Global Ionosphere-Thermosphere Model: Solar cycle, seasonal, and diurnal variations of the Mars upper atmosphere. *Journal of Geophysical Research: Planets*, 120(2), 311–342. <https://doi.org/10.1002/2014je004715>
- Brain, D. A., Mitchell, D. L., & Halekas, J. S. (2006). The magnetic field draping direction at Mars from April 1999 through August 2004. *Icarus*, 182(2), 464–473. <https://doi.org/10.1016/j.icarus.2005.09.023>
- Breus, T., Krymskii, A., Lundin, R., Dubinin, E., Luhmann, J., Yeroshenko, Y. G., et al. (1991). The solar wind interaction with Mars: Consideration of Phobos 2 mission observations of an ion composition boundary on the dayside. *Journal of Geophysical Research*, 96(A7), 11165–11174. <https://doi.org/10.1029/91ja01131>
- Brinca, A. (1991). Cometary linear instabilities: From profusion to perspective. *Cometary Plasma Processes*, 61, 211–221. <https://doi.org/10.1029/gm061p0211>
- Brinca, A. L., & Tsurutani, B. T. (1989). Influence of multiple ion species on low-frequency electromagnetic wave instabilities. *Journal of Geophysical Research*, 94(A10), 13565–13569. <https://doi.org/10.1029/ja094ia10p13565>
- Burgess, D., Lucek, E., Scholer, M., Bale, S., Balikhin, M., Balogh, A., et al. (2005). Quasi-parallel shock structure and processes. *Space Science Reviews*, 118(1), 205–222. <https://doi.org/10.1007/s11214-005-3832-3>
- Chaffin, M. S., Fowler, C. M., Deighan, J., Jain, S., Holsclaw, G., Hughes, A., et al. (2022). Patchy proton aurora at Mars: A global view of solar wind precipitation across the Martian dayside from EMM/EMUS. *Geophysical Research Letters*, 49(17), e2022GL099881. <https://doi.org/10.1029/2022gl099881>
- Chang, Q., Xu, X., Xu, Q., Wang, J., Xu, J., Ye, Y., & Zhang, T. (2020). The demagnetization of the Venusian ionosphere under nearly flow-aligned interplanetary magnetic fields. *The Astrophysical Journal*, 900(1), 63. <https://doi.org/10.3847/1538-4357/aba62a>
- Chapman, S., & Dunlop, M. (1986). Ordering of momentum transfer along  $V \wedge B$  in the AMPTE solar wind releases. *Journal of Geophysical Research*, 91(A7), 8051–8055. <https://doi.org/10.1029/ja091ia07p08051>
- Coates, A. (2004). Ion pickup at comets. *Advances in Space Research*, 33(11), 1977–1988. <https://doi.org/10.1016/j.asr.2003.06.029>
- Collinson, G., Sibeck, D., Omid, N., Frahm, R., Zhang, T., Mitchell, D., et al. (2020). Foreshock cavities at Venus and Mars. *Journal of Geophysical Research: Space Physics*, 125(8), e2020JA028023. <https://doi.org/10.1029/2020ja028023>
- Collinson, G., Wilson, L. B., III, Omid, N., Sibeck, D., Espley, J., Fowler, C. M., et al. (2018). Solar wind induced waves in the skies of Mars: Ionospheric compression, energization, and escape resulting from the impact of ultralow frequency magnetosonic waves generated upstream of the Martian bow shock. *Journal of Geophysical Research: Space Physics*, 123(9), 7241–7256. <https://doi.org/10.1029/2018ja025414>
- Connerney, J., Espley, J., Lawton, P., Murphy, S., Odom, J., Oliverson, R., & Sheppard, D. (2015). The MAVEN magnetic field investigation. *Space Science Reviews*, 195(1), 257–291. <https://doi.org/10.1007/s11214-015-0169-4>
- Cravens, T., Lindgren, C., & Puhl, P. (1995). The comet Halley diamagnetic cavity boundary. *Advances in Space Research*, 16(4), 19–24. [https://doi.org/10.1016/0273-1177\(95\)00203-q](https://doi.org/10.1016/0273-1177(95)00203-q)
- Cravens, T. E. (1987). Theory and observations of cometary ionospheres. *Advances in Space Research*, 7(12), 147–158. [https://doi.org/10.1016/0273-1177\(87\)90212-2](https://doi.org/10.1016/0273-1177(87)90212-2)
- Crider, D. H., Brain, D. A., Acuña, M. H., Vignes, D., Mazelle, C., & Bertucci, C. (2004). Mars Global Surveyor observations of solar wind magnetic field draping around Mars. In *Mars' magnetism and its interaction with the solar wind* (pp. 203–221). Springer.
- Deighan, J., Chaffin, M., Chaufray, J.-Y., Stewart, A. I. F., Schneider, N., Jain, S. K., et al. (2015). MAVEN IUVS observation of the hot oxygen corona at Mars. *Geophysical Research Letters*, 42(21), 9009–9014. <https://doi.org/10.1002/2015gl065487>
- Delva, M., Bertucci, C., Volwerk, M., Lundin, R., Mazelle, C., & Romanelli, N. (2015). Upstream proton cyclotron waves at Venus near solar maximum. *Journal of Geophysical Research: Space Physics*, 120(1), 344–354. <https://doi.org/10.1002/2014ja020318>

- Delva, M., Mazelle, C., Bertucci, C., Volwerk, M., Vörös, Z., & Zhang, T. (2011). Proton cyclotron wave generation mechanisms upstream of Venus. *Journal of Geophysical Research*, *116*(A2). <https://doi.org/10.1029/2010ja015826>
- Du, J., Zhang, T., Wang, C., Volwerk, M., Delva, M., & Baumjohann, W. (2009). Magnetosheath fluctuations at Venus for two extreme orientations of the interplanetary magnetic field. *Geophysical Research Letters*, *36*(9), L09102. <https://doi.org/10.1029/2009gl037725>
- Dubinin, E., Fraenz, M., Fedorov, A., Lundin, R., Edberg, N., Duru, F., & Vaisberg, O. (2011). Ion energization and escape on Mars and Venus. In *The plasma environment of Venus, Mars, and Titan* (pp. 173–211). Springer.
- Dubinin, E., Fränz, M., Woch, J., Roussos, E., Barabash, S., Lundin, R., et al. (2006). Plasma morphology at Mars. ASPERA-3 observations. *Space Science Reviews*, *126*(1), 209–238. <https://doi.org/10.1007/s11214-006-9039-4>
- Dubinin, E., Modolo, R., Fraenz, M., Woch, J., Duru, F., Akalin, F., et al. (2008). Structure and dynamics of the solar wind/ionosphere interface on Mars: MEX-ASPERA-3 and MEX-MARSIS observations. *Geophysical Research Letters*, *35*(11), L11103. <https://doi.org/10.1029/2008gl033730>
- Dubinin, E., Sauer, K., Lundin, R., Norberg, O., Trotignon, J.-G., Schwingenschuh, K., et al. (1996). Plasma characteristics of the boundary layer in the Martian magnetosphere. *Journal of Geophysical Research*, *101*(A12), 27061–27075. <https://doi.org/10.1029/96ja02021>
- Dubinin, E., Winningham, D., Fränz, M., Woch, J., Lundin, R., Barabash, S., et al. (2006). Solar wind plasma protrusion into the Martian magnetosphere: ASPERA-3 observations. *Icarus*, *182*(2), 343–349. <https://doi.org/10.1016/j.icarus.2005.08.023>
- Duru, F., Gurnett, D., Frahm, R., Winningham, J., Morgan, D., & Howes, G. (2009). Steep, transient density gradients in the Martian ionosphere similar to the ionopause at Venus. *Journal of Geophysical Research*, *114*(A12), A12310. <https://doi.org/10.1029/2009ja014711>
- Elphic, R., Russell, C., Slavin, J., & Brace, L. (1980). Observations of the dayside ionopause and ionosphere of Venus. *Journal of Geophysical Research*, *85*(A13), 7679–7696. <https://doi.org/10.1029/ja085ia13p07679>
- Ergun, R., Andersson, L., Fowler, C., & Thaller, S. (2021). Kinetic modeling of Langmuir probes in space and application to the MAVEN Langmuir probe and waves instrument. *Journal of Geophysical Research: Space Physics*, *126*(3), e2020JA028956. <https://doi.org/10.1029/2020ja028956>
- Ergun, R., Andersson, L., Fowler, C., Thaller, S., & Yelle, R. (2021). Situ measurements of electron temperature and density in Mars' dayside ionosphere. *Geophysical Research Letters*, *48*(14), e2021GL093623. <https://doi.org/10.1029/2021gl093623>
- Ergun, R., Morooka, M., Andersson, L., Fowler, C., Delory, G., Andrews, D. J., et al. (2015). Dayside electron temperature and density profiles at Mars: First results from the MAVEN Langmuir probe and waves instrument. *Geophysical Research Letters*, *42*(21), 8846–8853. <https://doi.org/10.1002/2015gl065280>
- Fang, X., Ma, Y., Luhmann, J., Dong, Y., Brain, D., Hurley, D., et al. (2018). The morphology of the solar wind magnetic field draping on the dayside of Mars and its variability. *Geophysical Research Letters*, *45*(8), 3356–3365. <https://doi.org/10.1002/2018gl077230>
- Fowler, C., Andersson, L., Ergun, R., Harada, Y., Hara, T., Collinson, G., et al. (2018). MAVEN observations of solar wind-driven magnetosonic waves heating the Martian dayside ionosphere. *Journal of Geophysical Research: Space Physics*, *123*(5), 4129–4149. <https://doi.org/10.1029/2018ja025208>
- Fowler, C., McFadden, J., Hanley, K., Mitchell, D., Curry, S., & Jakosky, B. (2022). In-situ measurements of ion density in the Martian ionosphere: Underlying structure and variability observed by the MAVEN-STATIC instrument. *Journal of Geophysical Research: Space Physics*, *127*(8), e2022JA030352. <https://doi.org/10.1029/2022ja030352>
- Fowler, C. M., Halekas, J., Schwartz, S., Goodrich, K., Gruesbeck, J., & Benna, M. (2019). The modulation of solar wind hydrogen deposition in the Martian atmosphere by foreshock phenomena. *Journal of Geophysical Research: Space Physics*, *124*(8), 7086–7097. <https://doi.org/10.1029/2019ja026938>
- Fowler, C. M., Hanley, K. G., McFadden, J. P., Chaston, C. C., Bonnell, J. W., Halekas, J. S., et al. (2021). MAVEN observations of low frequency steepened magnetosonic waves and associated heating of the Martian nightside ionosphere. *Journal of Geophysical Research: Space Physics*, *126*(10), e2021JA029615. <https://doi.org/10.1029/2021ja029615>
- Fox, J. L., & Hać, A. B. (2009). Photochemical escape of oxygen from Mars: A comparison of the exobase approximation to a Monte Carlo method. *Icarus*, *204*(2), 527–544. <https://doi.org/10.1016/j.icarus.2009.07.005>
- Gary, S. P. (1991). Electromagnetic ion/ion instabilities and their consequences in space plasmas: A review. *Space Science Reviews*, *56*(3), 373–415. <https://doi.org/10.1007/bf00196632>
- Gary, S. P. (1993). *Theory of space plasma microinstabilities* (Vol. 7). Cambridge University Press.
- Gary, S. P., Akimoto, K., & Winske, D. (1989). Computer simulations of cometary-ion/ion instabilities and wave growth. *Journal of Geophysical Research*, *94*(A4), 3513–3525. <https://doi.org/10.1029/ja094ia04p03513>
- Glassmeier, K.-H., Coates, A., Acuna, M., Goldstein, M., Johnstone, A., Neubauer, F., & Reme, H. (1989). Spectral characteristics of low-frequency plasma turbulence upstream of comet P/Halley. *Journal of Geophysical Research*, *94*(A1), 37–48. <https://doi.org/10.1029/ja094ia01p00037>
- Goetz, C., Koenders, C., Hansen, K., Burch, J., Carr, C., Eriksson, A., et al. (2016). Structure and evolution of the diamagnetic cavity at comet 67P/Churyumov–Gerasimenko. *Monthly Notices of the Royal Astronomical Society*, *462*(Suppl 1), S459–S467. <https://doi.org/10.1093/mnras/stw3148>
- Goetz, C., Koenders, C., Richter, I., Altwegg, K., Burch, J., Carr, C., et al. (2016). First detection of a diamagnetic cavity at comet 67P/Churyumov–Gerasimenko. *Astronomy & Astrophysics*, *588*, A24. <https://doi.org/10.1051/0004-6361/201527728>
- Halekas, J. (2017). Seasonal variability of the hydrogen exosphere of Mars. *Journal of Geophysical Research: Planets*, *122*(5), 901–911. <https://doi.org/10.1002/2017je005306>
- Halekas, J., Brain, D., Luhmann, J., DiBraccio, G., Ruhunusiri, S., Harada, Y., et al. (2017). Flows, fields, and forces in the Mars-solar wind interaction. *Journal of Geophysical Research: Space Physics*, *122*(11), 11–320. <https://doi.org/10.1002/2017ja024772>
- Halekas, J., Lillis, R., Mitchell, D., Cravens, T., Mazelle, C., Connerney, J., et al. (2015). MAVEN observations of solar wind hydrogen deposition in the atmosphere of Mars. *Geophysical Research Letters*, *42*(21), 8901–8909. <https://doi.org/10.1002/2015gl064693>
- Halekas, J., Taylor, E., Dalton, G., Johnson, G., Curtis, D., McFadden, J., et al. (2015). The solar wind ion analyzer for MAVEN. *Space Science Reviews*, *195*(1), 125–151. <https://doi.org/10.1007/s11214-013-0029-z>
- Hamre, B., Hansen, J., & Kocbach, L. (1999). Cross sections for capture, excitation and ionization in proton-oxygen collisions. *Journal of Physics B: Atomic, Molecular and Optical Physics*, *32*(6), L127–L131. <https://doi.org/10.1088/0953-4075/32/6/001>
- Harada, Y., Andersson, L., Fowler, C., Mitchell, D., Halekas, J., Mazelle, C., et al. (2016). MAVEN observations of electron-induced whistler mode waves in the Martian magnetosphere. *Journal of Geophysical Research: Space Physics*, *121*(10), 9717–9731. <https://doi.org/10.1002/2016ja023194>
- Henderson, S., Halekas, J., Lillis, R., & Elrod, M. (2021). Precipitating solar wind hydrogen as observed by the MAVEN spacecraft: Distribution as a function of column density, altitude, and solar zenith angle. *Journal of Geophysical Research: Planets*, *126*(7), e2020JE006725. <https://doi.org/10.1029/2020je006725>

- Holmberg, M. K., Andre, N., Garnier, P., Modolo, R., Andersson, L., Halekas, J., et al. (2019). MAVEN and MEX multi-instrument study of the dayside of the Martian induced magnetospheric structure revealed by pressure analyses. *Journal of Geophysical Research: Space Physics*, *124*(11), 8564–8589. <https://doi.org/10.1029/2019ja026954>
- Ip, W.-H., & Axford, W. (1986). The acceleration of particles in the vicinity of comets. *Planetary and Space Science*, *34*(11), 1061–1065. [https://doi.org/10.1016/0032-0633\(86\)90016-4](https://doi.org/10.1016/0032-0633(86)90016-4)
- Jakosky, B. M., Lin, R. P., Grebowsky, J. M., Luhmann, J. G., Mitchell, D., Beutelschies, G., et al. (2015). The Mars atmosphere and volatile evolution (MAVEN) mission. *Space Science Reviews*, *195*(1), 3–48. <https://doi.org/10.1007/s11214-015-0139-x>
- Jakosky, B. M., Slipski, M., Benna, M., Mahaffy, P., Elrod, M., Yelle, R., et al. (2017). Mars' atmospheric history derived from upper-atmosphere measurements of  $^{38}\text{Ar}/^{36}\text{Ar}$ . *Science*, *355*(6332), 1408–1410. <https://doi.org/10.1126/science.aai7721>
- Liu, D., Rong, Z., Gao, J., He, J., Klinger, L., Dunlop, M. W., et al. (2021). Statistical properties of solar wind upstream of Mars: MAVEN observations. *The Astrophysical Journal*, *911*(2), 113. <https://doi.org/10.3847/1538-4357/abed50>
- López-Patiño, J., Fuentes, B., Yousif, F., & Martínez, H. (2015). Relative differential cross section measurements in  $\text{H}^+$ - $\text{CO}_2$  low energy collisions. *International Journal of Physics*, *3*(2), 23–35. <https://doi.org/10.15640/ijpa.v3n2a2>
- Luhmann, J., & Cravens, T. (1991). Magnetic fields in the ionosphere of Venus. *Space Science Reviews*, *55*(1), 201–274. <https://doi.org/10.1007/bf00177138>
- Luhmann, J., & Kozyra, J. (1991). Dayside pickup oxygen ion precipitation at Venus and Mars: Spatial distributions, energy deposition and consequences. *Journal of Geophysical Research*, *96*(A4), 5457–5467. <https://doi.org/10.1029/90ja01753>
- Mahaffy, P. R., Benna, M., King, T., Harpole, D. N., Arvey, R., Barciniak, M., et al. (2015). The neutral gas and ion mass spectrometer on the Mars atmosphere and volatile evolution mission. *Space Science Reviews*, *195*(1), 49–73. <https://doi.org/10.1007/s11214-014-0091-1>
- Matsunaga, K., Seki, K., Brain, D. A., Hara, T., Masunaga, K., McFadden, J. P., et al. (2017). Statistical study of relations between the induced magnetosphere, ion composition, and pressure balance boundaries around Mars based on MAVEN observations. *Journal of Geophysical Research: Space Physics*, *122*(9), 9723–9737. <https://doi.org/10.1002/2017ja024217>
- Mazelle, C., Winterhalter, D., Sauer, K., Trotignon, J., Acuna, M., Baumgärtel, K., et al. (2004). Bow shock and upstream phenomena at Mars. *Space Science Reviews*, *111*(1), 115–181. <https://doi.org/10.1023/b:spac.0000032717.98679.d0>
- McComas, D. J., Spence, H. E., Russell, C., & Saunders, M. (1986). The average magnetic field draping and consistent plasma properties of the Venus magnetotail. *Journal of Geophysical Research*, *91*(A7), 7939–7953. <https://doi.org/10.1029/ja091ia07p07939>
- McFadden, J., Kortmann, O., Curtis, D., Dalton, G., Johnson, G., Abiad, R., et al. (2015). MAVEN suprathermal and thermal ion composition (STATIC) instrument. *Space Science Reviews*, *195*(1–4), 199–256. <https://doi.org/10.1007/s11214-015-0175-6>
- Mitchell, D., Mazelle, C., Sauvaud, J.-A., Thocaven, J.-J., Rouzaud, J., Fedorov, A., et al. (2016). The MAVEN solar wind electron analyzer. *Space Science Reviews*, *200*(1), 495–528. <https://doi.org/10.1007/s11214-015-0232-1>
- Moses, S., Coroniti, F., & Scarf, F. (1988). Expectations for the microphysics of the Mars-solar wind interaction. *Geophysical Research Letters*, *15*(5), 429–432. <https://doi.org/10.1029/g1015i005p00429>
- Nagy, A., Winterhalter, D., Sauer, K., Cravens, T., Brecht, S., Mazelle, C., et al. (2004). The plasma environment of Mars. *Space Science Reviews*, *111*(1), 33–114. <https://doi.org/10.1023/b:spac.0000032718.47512.92>
- Nier, A., & McElroy, M. B. (1977). Composition and structure of Mars' upper atmosphere: Results from the neutral mass spectrometers on Viking 1 and 2. *Journal of Geophysical Research*, *82*(28), 4341–4349. <https://doi.org/10.1029/jf082i028p04341>
- Omid, N., Collinson, G., & Sibeck, D. (2017). Structure and properties of the foreshock at Venus. *Journal of Geophysical Research: Space Physics*, *122*(10), 10–275. <https://doi.org/10.1002/2017ja024180>
- Pandey, M., Dubey, R., & Tripathi, D. (2007). Charge transfer in keV proton collision with atomic oxygen: Differential and total cross sections. *The European Physical Journal D*, *45*(2), 273–277. <https://doi.org/10.1140/epjd/e2007-00262-x>
- Phillips, J., Luhmann, J., & Russell, C. (1986). Magnetic configuration of the Venus magnetosheath. *Journal of Geophysical Research*, *91*(A7), 7931–7938. <https://doi.org/10.1029/ja091ia07p07931>
- Rahmati, A., Larson, D., Cravens, T., Lillis, R., Halekas, J., McFadden, J., et al. (2017). MAVEN measured oxygen and hydrogen pickup ions: Probing the Martian exosphere and neutral escape. *Journal of Geophysical Research: Space Physics*, *122*(3), 3689–3706. <https://doi.org/10.1002/2016ja023371>
- Ramstad, R., Brain, D. A., Dong, Y., Espley, J., Halekas, J., & Jakosky, B. (2020). The global current systems of the Martian induced magnetosphere. *Nature Astronomy*, *4*(10), 979–985. <https://doi.org/10.1038/s41550-020-1099-y>
- Roeten, K. J., Bougher, S. W., Benna, M., Mahaffy, P. R., Lee, Y., Pawlowski, D., et al. (2019). MAVEN/NGIMS thermospheric neutral wind observations: Interpretation using the M-GITM general circulation model. *Journal of Geophysical Research: Planets*, *124*(12), 3283–3303. <https://doi.org/10.1029/2019je005957>
- Romanelli, N., Mazelle, C., Chaufray, J.-Y., Meziane, K., Shan, L., Ruhunusiri, S., et al. (2016). Proton cyclotron waves occurrence rate upstream from Mars observed by MAVEN: Associated variability of the Martian upper atmosphere. *Journal of Geophysical Research: Space Physics*, *121*(11), 11113–11128. <https://doi.org/10.1002/2016ja023270>
- Ruhunusiri, S., Halekas, J., Connerney, J., Espley, J., McFadden, J., Larson, D., et al. (2015). Low-frequency waves in the Martian magnetosphere and their response to upstream solar wind driving conditions. *Geophysical Research Letters*, *42*(21), 8917–8924. <https://doi.org/10.1002/2015gl064968>
- Ruhunusiri, S., Halekas, J., Espley, J., Mazelle, C., Brain, D., Harada, Y., et al. (2017). Characterization of turbulence in the Mars plasma environment with MAVEN observations. *Journal of Geophysical Research: Space Physics*, *122*(1), 656–674. <https://doi.org/10.1002/2016ja023456>
- Sánchez-Cano, B., Narvaez, C., Lester, M., Mendillo, M., Mayyasi, M., Holmstrom, M., et al. (2020). Mars' ionopause: A matter of pressures. *Journal of Geophysical Research: Space Physics*, *125*(9), e2020JA028145. <https://doi.org/10.1029/2020ja028145>
- Sauer, K., Bogdanov, A., & Baumgärtel, K. (1995). The protonopause—An ion composition boundary in the magnetosheath of comets, Venus and Mars. *Advances in Space Research*, *16*(4), 153–158. [https://doi.org/10.1016/0273-1177\(95\)00223-2](https://doi.org/10.1016/0273-1177(95)00223-2)
- Scholer, M., & Terasawa, T. (1990). Ion reflection and dissipation at quasi-parallel collisionless shocks. *Geophysical Research Letters*, *17*(2), 119–122. <https://doi.org/10.1029/g1017i002p00119>
- Schunk, R., & Nagy, A. (2009). *Ionospheres: Physics, plasma physics, and chemistry*. Cambridge University Press.
- Schwartz, S. J., & Burgess, D. (1991). Quasi-parallel shocks: A patchwork of three-dimensional structures. *Geophysical Research Letters*, *18*(3), 373–376. <https://doi.org/10.1029/91gl00138>
- Shan, L., Ge, Y., & Du, A. (2020). A case study of large-amplitude ULF waves in the Martian foreshock. *Earth and Planetary Physics*, *4*(1), 45–50. <https://doi.org/10.26464/epp2020004>
- Shan, L., Lu, Q., Wu, M., Gao, X., Huang, C., Zhang, T., & Wang, S. (2014). Transmission of large-amplitude ULF waves through a quasi-parallel shock at Venus. *Journal of Geophysical Research: Space Physics*, *119*(1), 237–245. <https://doi.org/10.1002/2013ja019396>

- Szegő, K., Glassmeier, K.-H., Bingham, R., Bogdanov, A., Fischer, C., Haerendel, G., et al. (2000). Physics of mass loaded plasmas. *Space Science Reviews*, 94(3), 429–671. <https://doi.org/10.1023/a:1026568530975>
- Torrence, C., & Compo, G. P. (1998). A practical guide to wavelet analysis. *Bulletin of the American Meteorological Society*, 79(1), 61–78. [https://doi.org/10.1175/1520-0477\(1998\)079<0061:apgtwa>2.0.co;2](https://doi.org/10.1175/1520-0477(1998)079<0061:apgtwa>2.0.co;2)
- Tsurutani, B. T., Page, D. E., Smith, E. J., Goldstein, B. E., Brinca, A. L., Thorne, R. M., et al. (1989). Low-frequency plasma waves and ion pitch angle scattering at large distances ( $>3.5 \times 10^5$  km) from Giacobini-Zinner: Interplanetary magnetic field  $\alpha$  dependences. *Journal of Geophysical Research*, 94(A1), 18–28. <https://doi.org/10.1029/ja094ia01p00018>
- Tsurutani, B. T., & Smith, E. J. (1986). Strong hydromagnetic turbulence associated with comet Giacobini-Zinner. *Geophysical Research Letters*, 13(3), 259–262. <https://doi.org/10.1029/g1013i003p00259>
- Tsurutani, B. T., Thorne, R. M., Smith, E. J., Gosling, J., & Matsumoto, H. (1987). Steepened magnetosonic waves at comet Giacobini-Zinner. *Journal of Geophysical Research*, 92(A10), 11074–11082. <https://doi.org/10.1029/ja092ia10p11074>
- Vignes, D., Mazelle, C., Rme, H., Acuña, M., Connerney, J., Lin, R., et al. (2000). The solar wind interaction with Mars: Locations and shapes of the bow shock and the magnetic pile-up boundary from the observations of the MAG/ER Experiment onboard Mars Global Surveyor. *Geophysical Research Letters*, 27(1), 49–52. <https://doi.org/10.1029/1999gl010703>
- Vogt, M. F., Withers, P., Mahaffy, P. R., Benna, M., Elrod, M. K., Halekas, J. S., et al. (2015). Ionopause-like density gradients in the Martian ionosphere: A first look with MAVEN. *Geophysical Research Letters*, 42(21), 8885–8893. <https://doi.org/10.1002/2015gl065269>
- Xu, S., Liemohn, M. W., Dong, C., Mitchell, D. L., Bougher, S. W., & Ma, Y. (2016). Pressure and ion composition boundaries at Mars. *Journal of Geophysical Research: Space Physics*, 121(7), 6417–6429. <https://doi.org/10.1002/2016ja022644>
- Zhang, T., Du, J., Ma, Y., Lammer, H., Baumjohann, W., Wang, C., & Russell, C. (2009). Disappearing induced magnetosphere at Venus: Implications for close-in exoplanets. *Geophysical Research Letters*, 36(20), L20203. <https://doi.org/10.1029/2009gl040515>